Open access • Journal Article • DOI:10.1111/STR.12170

Optimised experimental characterisation of polymeric foam material using DIC and the Virtual Fields Method — Source link

Peng Wang, Fabrice Pierron, Marco Rossi, Pascal Lava ...+2 more authors

Institutions: Aalborg University, University of Southampton, Marche Polytechnic University, Katholieke Universiteit Leuven

Published on: 01 Feb 2016 - Strain (Wiley-Blackwell Publishing Ltd.)

Topics: Experimental uncertainty analysis

Accepted in Strain, 2015

OPTIMIZED EXPERIMENTAL CHARACTERIZATION OF POLYMERIC FOAM MATERIAL USING DIC AND THE VIRTUAL FIELDS METHOD

P. Wang[1*], F. Pierron[2], M. Rossi[3], P. Lava[4], O.T. Thomsen[2,1]
[1] Department of Mechanical and Manufacturing Engineering, Aalborg University, Denmark
[2] Faculty of Engineering and the Environment, University of Southampton, UK
[3] Università Politecnica delle Marche, Ancona, Italy
[4] Department of Materials Engineering, University of Leuven, Belgium
* Corresponding author (O.Thomsen@soton.ac.uk)

Keywords: *Full-field measurements, Digital Image Correlation, Virtual Fields Method, Polymeric foam, Experimental design*

Abstract

This article presents a methodology to optimize the design of a realistic mechanical test to characterize the material elastic stiffness parameters of an orthotropic PVC foam material in one single test. Two main experimental techniques were used in this study: Digital Image Correlation (DIC) and the Virtual Fields Method (VFM). The actual image recording process was mimicked by numerically generating a series of deformed synthetic images. Subsequent to this, the entire measurement and data processing procedure was simulated by processing the synthetic images using DIC and VFM algorithms. This procedure was used to estimate the uncertainty of the measurements (systematic and random errors) by including the most significant parameters of actual experiments, e.g. the geometric test configuration, the parameters of the DIC process and the noise. By using these parameters as design variables and by defining different error functions as object functions, an optimization study was performed to minimize the uncertainty of the material parameter identification and to select the optimal test parameters. The confidence intervals of the identified parameters were predicted based on systematic and random errors obtained from the simulations. The simulated experimental results have shown that averaging multiple images can lead to a significant reduction of the random error. An experimental determination of the elastic coefficient of a PVC foam material was conducted using the optimized test parameters obtained from the numerical study. The identified stiffness values matched well with data from previous tests but even more interesting was the fact that the experimental uncertainty intervals matched

reasonably well with the predictions of the simulations, which is a highly original result and probably the main outcome of the present paper.

Introduction

Cellular polymer closed cell foams are broadly used as core material in lightweight sandwich structures. Common polymer closed cell foams include PVC, PMI, PU or PET foams. Ideally, polymer foam core materials can be considered as homogenous isotropic materials. However, in practice most polymer foams display both heterogeneous and anisotropic material behaviour due to the density variations and directionality of foam cells developed during the manufacturing process. The orthotropic material behaviour of polymeric foams has been studied extensively in the literature [1-4]. Most of the studies rely on the use of several different testing methods including uniaxial tension, compression and shear, conducted along deformation measurements that are based on either point-wise or area-wise (averaged) measurement techniques like e.g. extensometers or strain gauges. More recent work by Zhang et al. [5] and Taher et al. [6] have characterized the cross linked PVC foam material Divinycell H100 using Digital Image Correlation (DIC). Both of these studies characterized the orthotropic properties of PVC foam and the obtained results were in good agreement with the datasheets from the manufacturer [7]. However, a significant amount of time and effort was spent on designing the different test specimen shapes needed to reach a uniform stress/strain state in the gauge area. With the development of full-field measurement techniques, several novel inverse techniques have been proposed to process the heterogeneous stress/strain fields to simultaneously identify the whole set of constitutive parameters, e.g. the finite element model updating technique [8], the constitutive equation gap method [9], and the Virtual Fields Method (VFM) [10].

The Virtual Fields Method allows characterization of the material properties directly from full-field measurements. This method takes advantage of the heterogeneous strain fields obtained through full-field

measurement techniques, such as Digital Image Correlation (DIC) [11], speckle pattern interferometry [12] or the grid method [13]. In elasticity, it was shown that it was possible to simultaneously identify the complete set of orthotropic stiffness parameters without the need for iterative finite element computations. Thus, the VFM is much less time consuming than classical finite element model updating methods. Since the heterogeneity of the strain fields plays an important role in the VFM identification, the accuracy of the identification of the elastic stiffness coefficients heavily depends on the test configuration as well as on the full-field measurement parameters such as camera noise, spatial resolution and smoothing levels. Therefore, the design of the experiment becomes a non-trivial issue when using the VFM technique. A methodology to optimize the test configuration for VFM identification was firstly proposed by Pierron et al. (2007) [14]. The idea was to find an optimized specimen length and orthotropic material axis angle so as to minimize a cost function based on the sensitivity to noise of the sought material stiffness components. Some time later, Syed-Muhammad et al. optimized the shape of a composite orthotropic plate in bending [15]. Recently, a refined test configuration design procedure was proposed by Rossi and Pierron [16]. The study used the grid method as the full-field technique and simulated the whole measurement and identification chain, including image forming and grid method algorithm. This study provided a significant improvement of the optimization procedure by introducing the many different types of error sources into the cost function. In particular, the effect of the spatial resolution of the full-field technique was correctly taken into account which was not the case in [14]. However, this approach was not validated experimentally. Also, it relied on the grid method (also known as sampling moiré) which is not so commonly used in the experimental mechanics community.

In a recent article, an experimental methodology to identify all the material stiffness parameters of a PVC foam material in one single test using Digital Image Correlation and the Virtual Fields Method was presented [17]. The study provided an optimized material test configuration with a particular objective of improving the accuracy of the identification. Although the selected test configuration led to a considerable improvement of the experimental results, significant differences were found between reference values of material parameters known

from literature and/or other tests and the experimental results from that study. It was thought that one of the reasons for this was that the conducted optimization study was based on finite element simulated strain fields which did not include the sources of error that arise from real DIC measurements. In particular, the low-pass spatial filtering effect of the DIC measurements will lead to underestimation of the strains in large strain gradient areas of the test specimen, which in turn will lead to biases on the identified stiffness components. Moreover, the low signal to noise ratio associated with the measurement of the elastic material properties of polymer foams will tend to increase the random error (scatter) of the data. Accordingly, a prerequisite for resolving the issues identified from the previous study ([17]), and thereby providing more accurate and robust materials parameter identification, is the establishment of a reasonable quantification of the uncertainty of the measurements as well as further improvement of the experiments. It must be noted that establishing realistic uncertainty bounds in identified material parameters from such inverse approaches is key to the diffusion of such techniques to industry in the future. This topic has very rarely been approached in the past and when so, only the random error was addressed but not the bias arising from the spatial low-pass filtering effect mentioned above.

In the present study, a procedure has been developed to realistically simulate the modified Arcan test for polymer foams [6] using Digital Image Correlation and the Virtual Fields Method. The idea is to construct deformed synthetic images using finite element (FE) displacements. From this, the reference and deformed synthetic images will be processed using Digital Image Correlation, and the Virtual Fields Method will be used subsequently to extract all the stiffness parameters. The uncertainty of the measurements, including the systematic and random errors, has been evaluated thoroughly by including several different sources of error. The systematic and random errors of the measurements were analyzed separatelby introducing two different error functions based on data with and without simulated camera noise. The optimization study was undertaken by using the loading angle and the off-axis angle of the material principal direction as the two design variables. By minimizing the uncertainty predicted from the error functions, an optimized test configuration has been identified. Subsequently, the influence of subset size and smoothing levels has been evaluated based on the

optimized test configuration. Moreover, an effective method to reduce the random error from the measurements has been proposed by studying the effect of image averaging, and an optimal number of images to be averaged has been identified. Finally, a detailed experimental validation has been conducted based on the optimized test parameters selected from the numerical study.

Simulation of the experimental procedure

Test setup and specimens

The experimental setup used to perform the foam characterization is represented in Figure 1. The test specimens were prepared using closed-cell cross-linked Divinycell H100 PVC foam panels manufactured by DIAB [7]. It has previously been established that this material displays orthotropic/transversely isotropic elastic properties due to the different elongations of the foam cells in the rising (through-thickness) and in-plane directions during the manufacturing process [5]. Since the aim of this study is to identify all the material properties in one single test, the experiments should be designed to induce balanced heterogeneous strain maps for all the components to be identified. A Modified Arcan test Fixture (MAF) was used to introduce various kinds of loading conditions (shown in Figure 1). This fixture was proposed recently to identify orthotropic material parameters [6]. The key characteristics of the MAF is that it enables the introduction of different combinations of shear, tensile and compression loads by connecting different loading holes to the two arms of the fixture. A simple 20 x 20 x 5 mm^3 flat square shaped foam specimen was selected to induce a heterogeneous strain field dominated by a combination of shear and longitudinal tensile stresses, while compressive stress concentrations occur near the ends of the bonded regions (interfaces between foam specimen and tabs – see Figure 1).

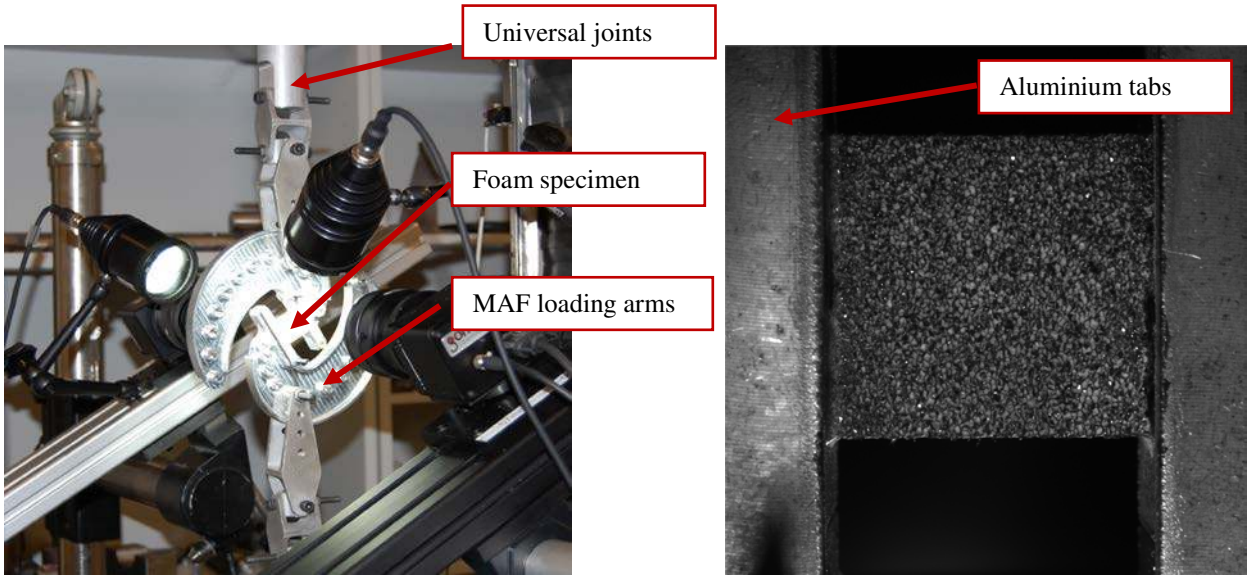

Figure 1: (a) 2D DIC measurement setup with MAF test fixture (b) test specimen bonded with the tabs

The material orthotropy axes are defined as the through-thickness (direction 1) and two in-plane directions (directions 2 and 3) of the original foam panels provided by the manufacturers (see Figure 2). In order to obtain a more complex multiaxial state of stress and strain and thereby activate all the orthotropic elastic stiffness components in the response of the material, specimens were prepared with different off-axis angles θ according to the material orthotropy directions (demonstrated in Figure 2). A 3-axis CNC milling machine was used to cut the specimens from the central part of a thick PVC foam panel to minimize the density variations that are typically experienced close to the top and bottom surfaces of PVC foam plates. Material direction 1 is the through-thickness direction and material direction 2 is the in plane direction (see Figure 2). After milling, the two sides of the foam specimens perpendicular to the x-axis were bonded to aluminium tabs using Araldite epoxy adhesive and inserted into the fixture.

2D digital image correlation was used to determine the in-plane displacement fields at the surface of the foam specimens under varying loading conditions. The reference and deformed randomly sprayed speckle patterns on both sides of the specimens were recorded by two 8 bits CCD cameras (2048 x 2048 pixel^2) with 50 mm lenses.

The cameras were rotated according to the loading angle of the specimen so that the displacements and strains were computed along the global coordinate direction of the specimen (x and y, see Figure 2). The images of both sides of the specimens can be captured by placing two cameras back to back. This experimental procedure was first proposed by Moulart *et al.* [18]. The advantage of this setup is that it enables the elimination of the effect of out-of-plane movements by averaging the measured values from the two cameras, and it can also account for possible through-thickness gradients of the strain field. This was already successfully employed in [6]. By dividing each image into many small computational units called facets or subsets, the displacement was computed at the centre of each facet by correlating the random speckle pattern. The strain components can then be obtained using numerical differentiation. The DIC software ‘‘MatchID’’ [19,20] was used to perform2D DIC between the deformed and undeformed images.

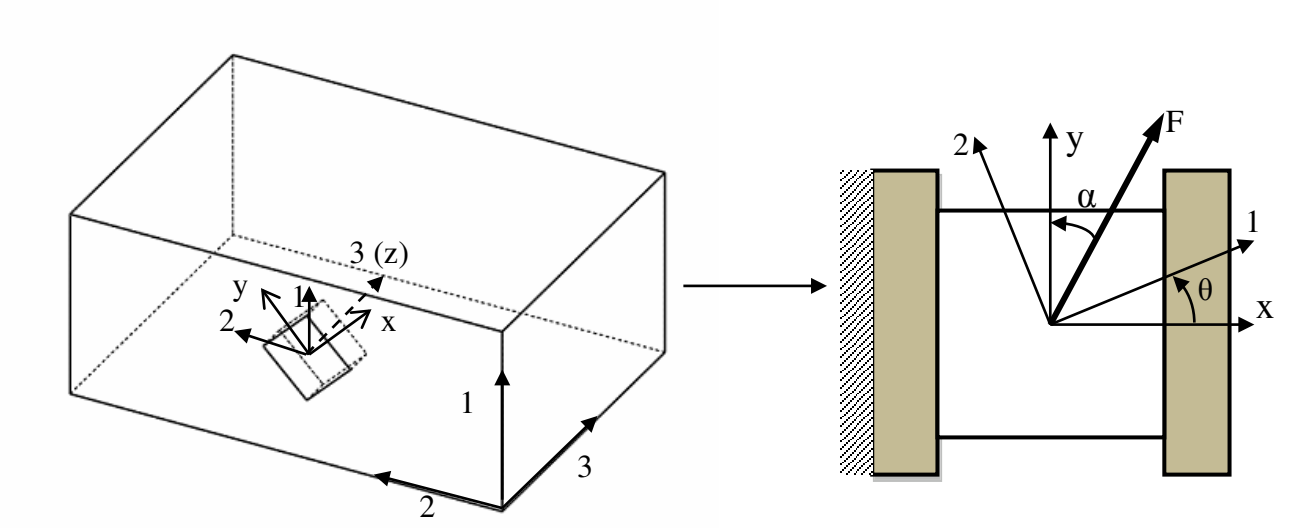

Figure 2: Schematic of the test – (1,2,3) are the material orthotropy axes, (x,y,z) are the coupon axes

Simulating the DIC measurements

An important step in this study is to simulate the digital image correlation process realistically. The procedure includes three steps: (1) Development of a finite element (FE) model to create the displacements field; (2)

Deformation of the reference images with displacements obtained from the FE analysis; (3) Digital image correlation between the reference and deformed synthetic images. The parametric FE analysis was performed using ANSYS version 14.0 along with the ANSYS APDL language to simulate the modified Arcan specimen response with different test configurations. The reference material properties (Q_{11}=143.4 MPa, Q_{22}=63.41 MPa, Q_{12}=26.01 MPa, Q_{66}=30.12 MPa) input into the FE model were obtained using conventional ASTM standard tests in [5]. The 2D plane stress model was built up using the PLANE 82 quadrilateral isoparametric element, with eight nodes and sixteen degrees of freedom (DOF). An FE mesh convergence study was performed to ensure that convergent FE models were used for the simulations.

The two arms of the Arcan fixture (see Figure 1) were simulated as rigid bodies in the FE model. The FE model includes two design variables; the first is the loading angle which can be adjusted by connecting to different holes in the modified Arcan fixture; the second is the material principal direction which can be varied (in the physical test specimens) by cutting the specimen in different directions within the foam slab. The FE simulated displacement fields were generated with different combinations of the two design variables. After obtaining the FE displacement fields, a synthetic deformation procedure of the speckle patterns was adopted to simulate the image recording process. The reference image, captured from one of the test specimens in real testing conditions, is shown in Figure 3(a). This reference image was deformed according to the displacement fields calculated from the FE model. The deformation process was performed numerically using an interpolation routine. This procedure is based on the 2D interpolation functions in Matlab. It has been proposed and validated previously [21]. Figure 3(b) shows an example of the deformed synthetic images using pure shear loading condition. The synthetic images were processed by the MatchID DIC software [19,20] to calculate the displacement fields, and the strain fields were subsequently derived using finite differences and subsequent Gaussian smoothing. Table 1 summarizes the parameters used for DIC.

Table 1: DIC parameters for the numerical study (MatchID DIC package).

Technique	2D image correlation
Subset size	Variable, to be precised for each set of results
Shift	50% of the subset size
Shape function	Affine
Interpolation function	Bicubic polynomial
Correlation criterion	Approximated Normalized Sum of Squared Difference (Approximated NSSD)
Pre-smoothing applied to the images	None
Camera	8 bit, 2048 x 2048 pixel^2
Field of view	24mm x 24mm
Noise	White Gaussian, standard deviation 1% of dynamic range (2.56 grey levels)
Strain field:	
Differentiation method	Finite differences
Smoothing method	Gaussian smoothing (kernel size variable, to be précised for each set of results)

Figure 4 shows the comparison between the simulated DIC and the FE strain maps calculated from Figure 3. The two sets of results display obvious differences at the corner areas of the specimen where high strain concentrations are present. Differences are mainly caused by the limitation in the spatial resolution of the DIC technique which does not enable to reproduce the high strain gradients at the corners. This problem is enhanced by increasing levels of smoothing, as illustrated on Figure 5.

This systematic reconstruction bias is an important source of error which has to be taken into account in order to predict the identification error realistically. Test configuration which results in more severe strain gradients, the low-pass filtering effect of DIC will be more critical and lead to significant errors in the parameter identification. A detailed study of this is presented in the following section.

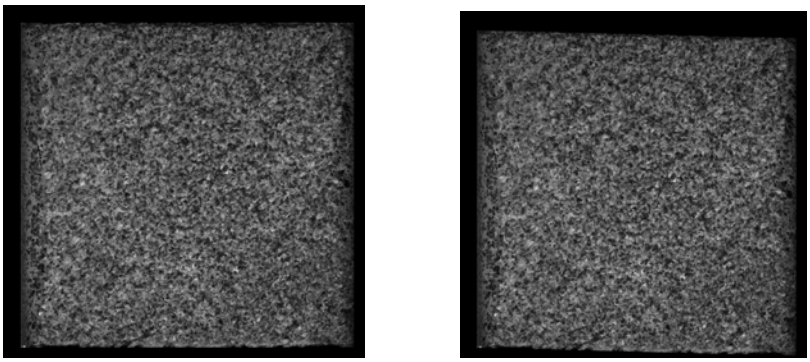

(a) (b)

Figure 3: (a) Reference image (size 1650 x 1650 pixel^2); (b) Deformed synthetic image for a vertical shear load

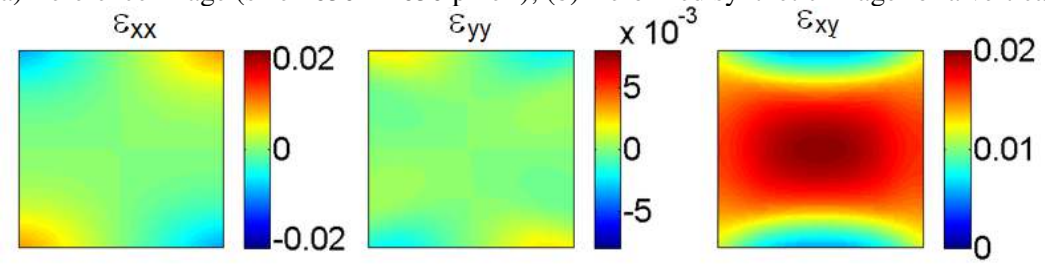

(a)

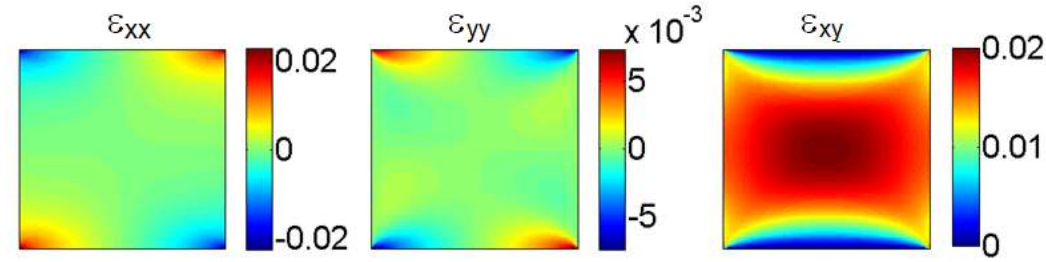

(b)

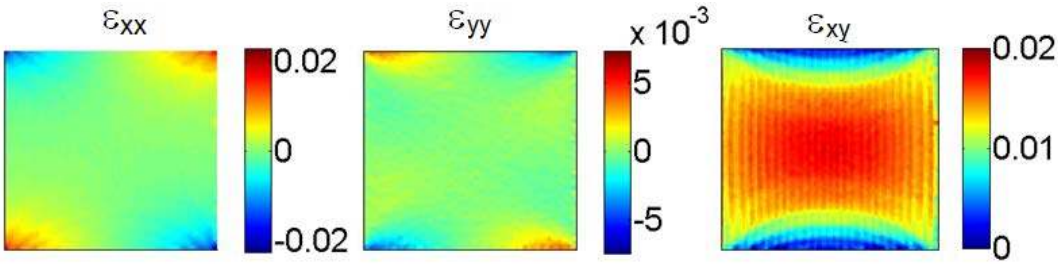

(c)

Figure 4: (a) Strain maps from DIC using synthetic images without noise (Subset size: 30, Gaussian kernel size: 10) (b) Strain maps from FE model (c) Strain maps from DIC using synthetic images without noise (Subset size: 30, Gaussian kernel size: 2)

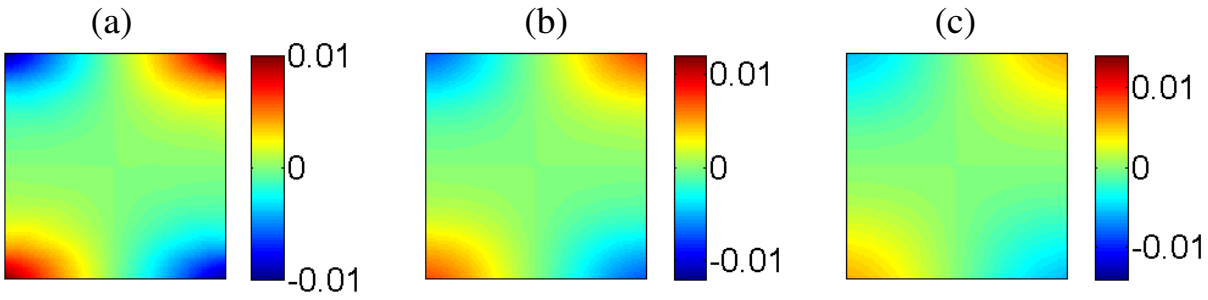

Figure 5: ε_{xx} strain maps with Gaussian kernel size of (a) 10 (b) 20 (c) 30

The Virtual Fields Method

After having obtained the strain fields from the simulated DIC procedure introduced above, the virtual fields method was used to extract the stiffness parameters from the synthetic strain maps. The VFM is based on the principle of virtual work, which can be expressed in the following form for quasi-static conditions and when body forces are neglected:

$$\int_V \sigma : \varepsilon^* dV = \int_{\partial V} \overline{T} \cdot u^* dS \tag{1}$$

where ':' denotes the contracted product of the stress tensor σ and the virtual strain tensor ε*, and '.' denotes the dot product between the external stress vector $\overline{T}$ and the virtual displacement vector u*. This equation expresses the condition of global equilibrium between the internal virtual work over the specimen volume V and the external virtual work over the boundary surface of V. The constitutive equation of the polymer foam, assuming plane stress orthotropic linear elasticity, can be written as (in the material orthotropy axes):

$$\begin{Bmatrix} \sigma_1 \\ \sigma_2 \\ \sigma_6 \end{Bmatrix} = \begin{bmatrix} Q_{11} & Q_{12} & 0 \\ Q_{12} & Q_{22} & 0 \\ 0 & 0 & Q_{66} \end{bmatrix} \begin{Bmatrix} \varepsilon_1 \\ \varepsilon_2 \\ \varepsilon_6 \end{Bmatrix} \tag{2}$$

where σ_i, ε_i, (i=1,2,6) are the in-plane stress and strain components according to the so-called contracted notation [22], and Q_{ij} (i,j=1,2,6) are the plane stress in-plane stiffness components. For an in-plane test with

constant specimen thickness assuming that the material is homogeneous over the field of view, equation (1) can be rewritten as:

$$Q_{11}t\int_S \varepsilon_1\varepsilon_1^* dS + Q_{22}t\int_S \varepsilon_2\varepsilon_2^* dS + Q_{12}t\int_S \left(\varepsilon_1\varepsilon_2^* + \varepsilon_2\varepsilon_1^*\right)dS + Q_{66}t\int_S \varepsilon_6\varepsilon_6^* dS = t\int_{Lf} \left(T_1u_1^* + T_2u_2^*\right)dl \quad (3)$$

where t is the thickness of the specimen. Since the elastic strain fields are known from the full-field measurement, and since the resulting force applied to the specimen is known from the load cell readings, a new set of equations can be obtained in which only the elastic parameters are unknown for each new selected virtual field. When choosing at least as many independent virtual fields as unknowns, all the parameters can be identified directly by solving the resulting linear system [10].

For the construction of the virtual fields, piecewise functions were used in this study. The details of the piecewise formulation of virtual fields can be found in [10, 23]. As a potentially infinite number of virtual fields can be written, an additional criterion was employed to select the virtual fields optimally and automatically aiming at minimizing noise influence on the identified parameters. The detailed derivation of this procedure is proposed in the optimized VFM theory [10, 24]. In the present study, bilinear shape functions with 4-noded quadrilateral elements have been used, and 4 x 4=16 virtual elements were employed giving a total of 50 virtual degrees of freedom (25 nodes with two virtual degrees of freedom each). A convergence study showed that a 4 x 4 virtual mesh was enough to provide stable identification and save computing time compared with a higher number of virtual elements.

For the modified Arcan test fixture used in this research [6] (see Figure 1), the measured data may be influenced by the adhesive or the shadow cast by the fixture. Therefore the surface of the test specimen is divided into three areas as shown in Figure 6: one area with actual deformation fields being measured (S_2) and two areas without actual strain field measurements (S_1 and S_3). S_2 is the central part of the specimen, whereas S1 and S3 are the outer left and right strips. Only the measurement area S_2 is taken into account in the VFM study (shown in Figure 4). The ratio between the length W of the field of view and the specimen length L is 0.8. It is important not to reduce this value too much as this would result in a loss of strain heterogeneity which would negatively impact the simultaneous identification of the complete set of stiffness components.

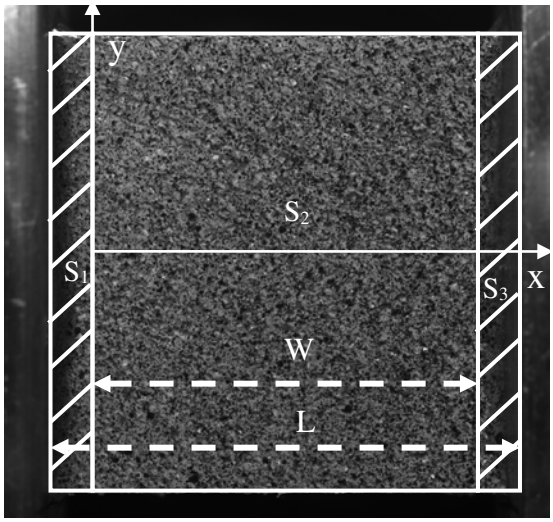

Figure 6: Measurement area S_2 used for identification (*W/L*=0.8)

As a consequence of the above, the virtual displacements on areas S_1 and S_3 are constrained to be rigid body-like so that missing experimental data on these two areas will not appear in the final equations (zero virtual strain fields cancelling out the virtual work of internal forces on S_1 and S_3). The virtual displacement on S_1 is selected to be zero. For S_3, only the resultant force F is measured and the virtual displacements have to be rigid body-like on S_3. Therefore, the horizontal and vertical virtual displacements over this area can be defined as constants a and b depending on α:

$$\begin{cases} a = \sin\alpha \\ b = \cos\alpha \end{cases} \tag{4}$$

This ensures that only the resultant force measured by the load cell is involved in the VFM equations (see [17]). The continuity conditions of the virtual displacement fields lead to the following constraints on the boundary of S_2 when automatically defining piecewise optimized virtual fields:

$$\begin{cases} u_1^{*(S_2)}(x=0,y)=0 \\ u_2^{*(S_2)}(x=0,y)=0 \\ u_1^{*(S_2)}(x=W,y)=a \\ u_2^{*(S_2)}(x=W,y)=b \end{cases} \tag{5}$$

More details of the derivation of the virtual boundary conditions can be found in [17]. This constrains 4 virtual degrees of freedom out of the 25 available. It is to be noted that the speciality condition used to define the virtual fields [10] constrains an additional 4 virtual degrees of freedom, hence a total of 17 available for the noise sensitivity optimization. As a rule of thumbs, this number should be between a few times the number of unknowns, which is the case here.

For the identification of the orthotropic material parameters, the strain and virtual strain fields obtained in the global coordinates x and y (see Figure 2) were transformed into the material principal directions 1 and 2 (Figure 2). The transformation relation is given in equations (6) and (7) below.

$$\begin{Bmatrix} \varepsilon_{11} \\ \varepsilon_{22} \\ \varepsilon_{12} \end{Bmatrix} = \begin{bmatrix} c^2 & s^2 & 2cs \\ s^2 & c^2 & -2cs \\ -2cs & 2cs & 2(c^2 - s^2) \end{bmatrix} \begin{Bmatrix} \varepsilon_{xx} \\ \varepsilon_{yy} \\ \varepsilon_{xy} \end{Bmatrix} \tag{6}$$

$$c = \cos\theta, s = \sin\theta \tag{7}$$

where θ is the off-axis angle relative to the material principal direction (see Figure 2).

Quantification of uncertainty and optimization study using simulated experiments

The long term objective of the present paper is to produce optimal test configurations to identify mechanical constitutive parameters from full-field measurements and inverse identification using the VFM. As seen in Figure 7 representing a flowchart of the present simulator, the identification quality depends on many parameters usually defined by the operator in an intuitive way (like which camera or which subset size to use) or even overlooked, like the shape functions or the interpolation functions, usually hidden in DIC commercial package, not to mention the speckle pattern often produced in a non-optimized nor reproducible manner with paint spray. If this new generation of test methods is to be used in industry in the future, it is essential to be able to define robust test procedures providing quantified uncertainty. To reach this goal, all parameters in the grey boxes (and there are others not mentioned here like the effect of lighting or the lens quality for instance) will

have to be set so as to produce the best possible results. It is to be noted that the definition of the test itself can be very complex while here, the variability has been restricted to the two loading and off-axis angles. At the moment, approaching this massive optimization problem with all parameters is out-of-reach. As a first step towards the final goal, the current study will focus on a few parameters thought to be part of the most influential: the subset size, the strain smoothing kernel as well as the two test design variables.

The GUM (Guide to the expression of Uncertainty in Measurement, [25]) considers two main sources of uncertainty: type A, which relates to the random part of the uncertainty and can be evaluated with statistical parameters and type B, which relates to systematic errors or biases. In Section 3.4.1, it is stated that '…the uncertainty of a measurement result is usually evaluated using a mathematical model of the measurement and the law of propagation of uncertainty.' This is exactly what is undertaken here. In the rest of the paper, type A uncertainty will be named 'random error' whereas type B will be called 'systematic error' or 'bias'.

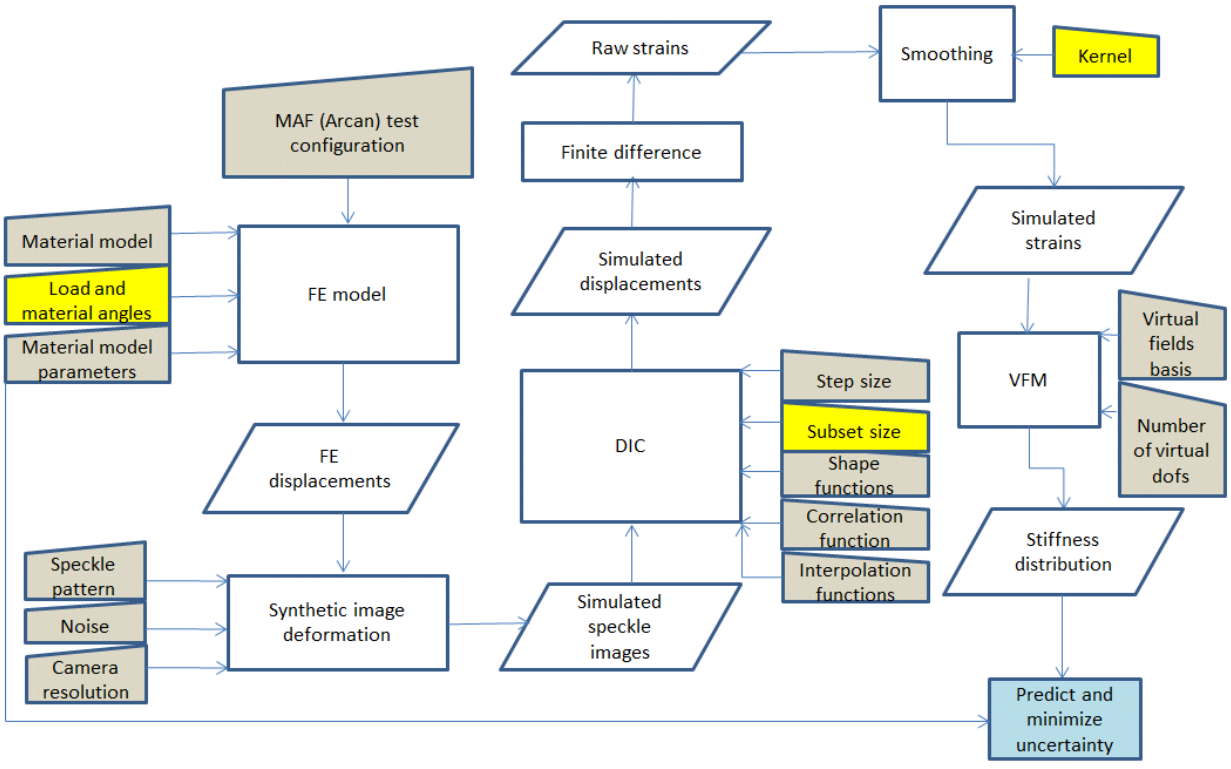

Figure 7: Flowchart of the identification simulator
(in grey, fixed parameters, in yellow, parameters studied here)

Two error functions were defined to evaluate the systematic and random errors separately. The hypothesis is that minimization of the systematic and random errors makes it possible to specify a set of design variables that will provide the best identification of the materials parameters. In order to simplify the problem, the optimization will be conducted in two steps. First, the two test design variables (the loading angle and the material principal direction) will be chosen to achieve the overall minimal systematic and random errors. After deciding on these, the optimization of the image processing parameters will be conducted to further improve the material parameter identification. The procedure is similar to the optimization study conducted on the test configurations except that DIC subset size and smoothing kernel size are considered as the new design variables while the test configuration has been selected based on the first step. Finally, an efficient method to reduce the random error is proposed, consisting in capturing multiple stabilized images and averaging them. An optimal number of images will be defined based on this study.

Test optimization based on the systematic error

By using the simulated experimental procedure described previously, a parametric study was conducted using different combinations of the two design variables of the test configuration (the material principal direction and the loading angle). The material principal direction (θ – see Figure 2) was varied between 0° to 90° with increments of 5°. The loading angle (α – see Figure 2) was also varied between 0° to 90° (from pure shear to pure tension) with increments of 15° according to the modified Arcan fixture, see Figures 1 and 2. By imposing the FE displacements on the reference speckle pattern, synthetic deformed images corresponding to different test configurations were produced. Since only the systematic error is considered in this section, noise was not added to the synthetic images. The reference and deformed synthetic images were processed by the DIC software run in batch mode to calculate the new simulated DIC displacement fields. A subset size of 30 x 30 was selected here. After this the strain maps were derived by numerical differentiation with Gaussian smoothing with kernel size of 10. Based on the tensile and shear stress vs. strain curves until failure obtained

from previous work [6], the strain maps are restricted to the linear elastic region of the PVC foam which is up to about 2% strain. These tensile and shear stress vs. strain curves were obtained **based conventional mechanical method** and have been attached in the Appendix of this article. In an actual test, the random error is highly dependent on the signal to noise ratio. Therefore, it is beneficial to have the largest strains possible. However, this is limited in practice by the fact that the material needs to remain linear elastic. Moreover, different test configurations (off-axis and load angles) lead to different stiffnesses so in order to provide unbiased comparison, it is necessary to normalize the applied load by a scaling factor k defined here as:

$$k = \max\left[\max\left|\frac{\varepsilon_x^i}{\varepsilon_x^{\max}}\right|, \max\left|\frac{\varepsilon_y^i}{\varepsilon_y^{\max}}\right|, \max\left|\frac{\varepsilon_{xy}^i}{\varepsilon_{xy}^{\max}}\right| \right] \tag{8}$$

where $\varepsilon_x^i, \varepsilon_y^i$ and ε_{xy}^i are the strain components at ith data point of the model. Max |.| is the maximum absolute value over all the data points. $\varepsilon_x^{\max}$, $\varepsilon_y^{\max}$ and $\varepsilon_{xy}^{\max}$ are the maximum allowable strain components for the material to remain linear elastic. These were obtained from previous experiments and reach up to 2% [6]. At the end, a VFM subroutine was used to extract the stiffness parameters from the simulated DIC results. The entire procedure described above was programmed using MATLAB®.

An error function C_1 has been introduced to evaluate the overall systematic error of the VFM identification. By minimizing this error function, the best test configuration can be identified. The error function C_1 is defined in eq. (9):

$$C_1(\alpha,\theta) = \frac{1}{4}\sum_{ij}\left(\frac{\left|Q_{ij} - Q_{ijref}\right|}{Q_{ijref}} \right) \tag{9}$$

where α is the loading angle, θ is the off-axis angle of the material principal direction, Q_{ijref} are the reference values of the four identified material stiffness parameters input into the FE model and Q_{ij} are the identified parameters from the simulated DIC measurements. This function represents an average identification bias over

the four stiffness components. The research reported in [17] indicated that missing data on the upper and bottom free edges of the specimen have a significant influence on the identified results due to the formulation of the Virtual Fields Method. A way to deal with this would be to do as with areas S_1 and S_3 (see Figure 6), i.e., assign rigid body-like virtual fields to the missing data areas on the free edges. But the continuity conditions imposed on the virtual displacements would then make it impossible to solve for the applied force in Eq. (3). Thus it would only be possible to identify stiffness ratios rather than the actual stiffness values. Therefore, missing data on the free edges were reconstructed in this study by copying the nearest data points to the missing data positions (padding). This was shown to be a very simple and efficient route to mitigating this issue [17].

The error function C_1 is plotted as a contour map with respect to the two design variables. The plots of the error function C_1 before and after the reconstruction are presented in Figure 8.

As can be observed from Figure 8, the reconstruction of the data at the edges significantly reduces the error for all test parameters. In the rest of the article, DIC data will systematically be reconstructed at the edges. When the off-axis angle θ is equal to 0° or 90° the identification errors are relatively large regardless of the value of the loading angle α. The reason for this is that the modified Arcan fixture only introduces tensile loading, shear loading or a combination of tensile and shear loading. With the off-axis angle θ near zero, the transverse stress/strain components are too small to enable stable identification of the transverse stiffness component. The good performance of the off-axis tensile test configuration (α=90°) confirms what has been found previously using the FE strain fields [17]. When comparing the identification procedures using either the strains directly from the FE model or the strains from the DIC simulation (Figure 9), it is clear that the latter produces much larger errors than the former. This is not surprising as the error generated by the DIC process is taken into account here, which provides a much more realistic evaluation of the identification error. It can also be seen that the plot in Figure 9(a) discriminates much better good from bad configuration. This fully justifies the current approach, showing that simplistic procedures based on FE strains do not produce realistic enough results. Finally, comparing Figures 8(b) and 9(a), it can be seen that increased smoothing significantly affects the resulting identification error, particularly in the low angles where bending is predominant and large strain

concentrations are present at the specimen corners. Nevertheless, parameters (α=90° and θ=25°) lead to minimal error with little effect of the increase of smoothing.

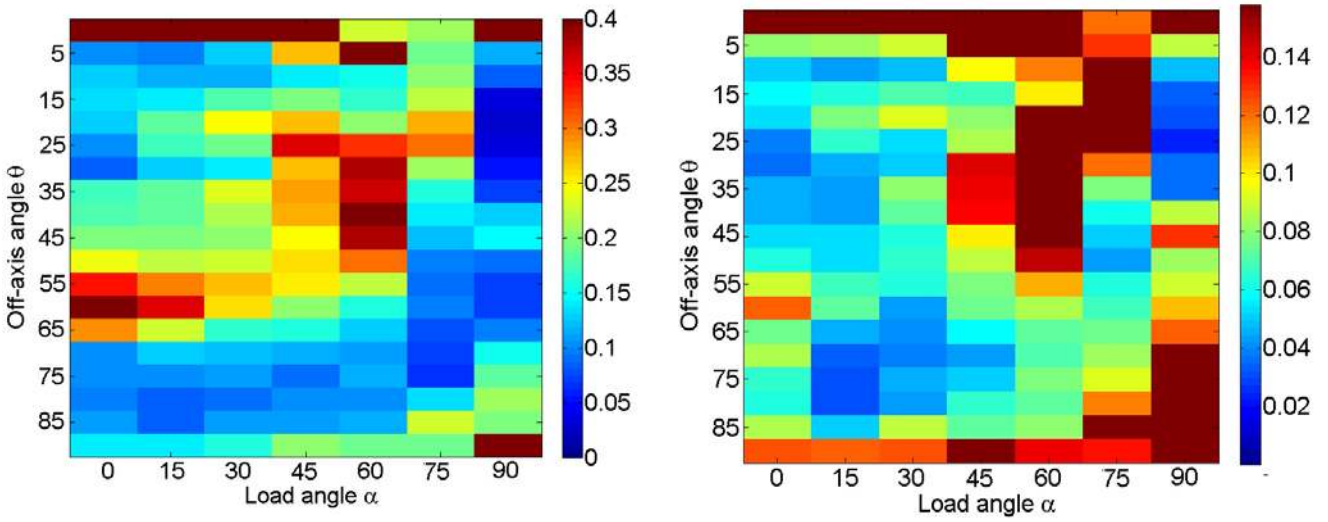

Figure 8: Error function C_1 before (a) and after (b) reconstructing missing data at the edges (using simulated DIC strain fields with subset 30 and Gaussian smoothing kernel size of 2)

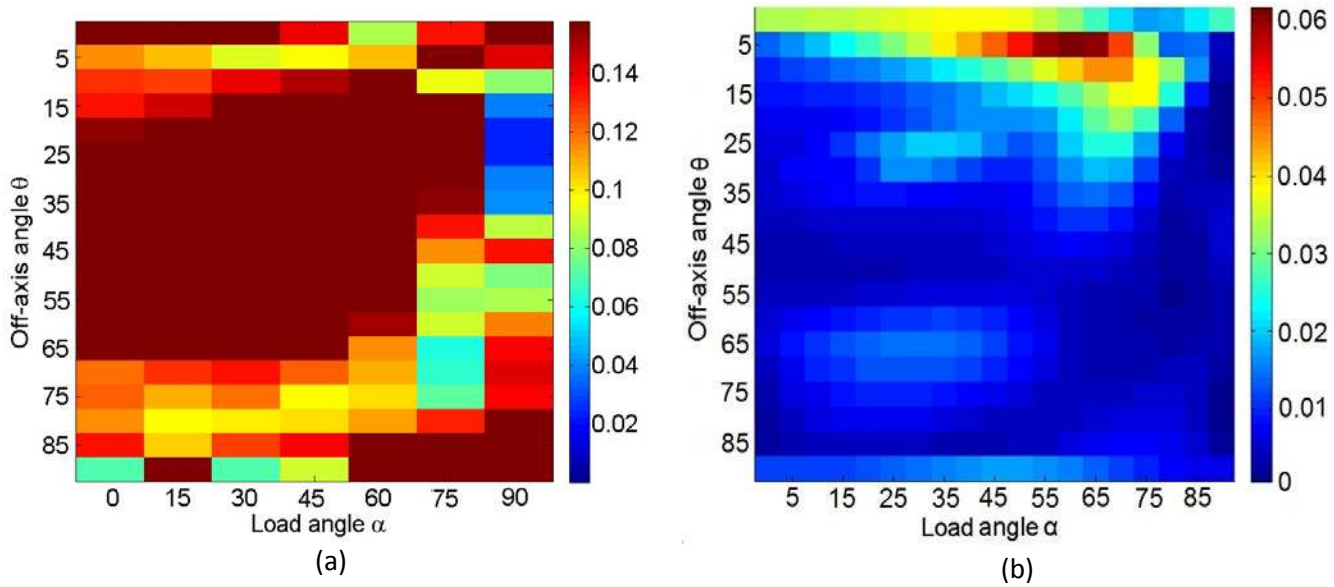

Figure 9: Error function C_1 from (a) DIC strain fields with subset 30 and Gaussian smoothing kernel size of 10 and (b) FE strains

As can be noted from Figures 8 and 9, several test configurations display very high identification errors. In order to investigate the cause of this phenomenon, the strain components of one of these test configurations (θ=5° and α=60°) have been compared with the strain components of the optimal test configuration (θ=25° and α=90°). It was found that the optimal test configuration exhibited lower strain gradients, especially for the strain components along the transverse direction as can be seen in Figure 10. For the test configuration with the highest identification errors (θ=5° and α=60° - Figure 10 (a)), strain values above 0.4% only occur at the corners of the specimen while most of the field of view exhibits very low strains. During the DIC process, large concentrated strains are significantly underestimated which in turn leads to a large bias in the VFM identification. This is demonstrated in Figure 11 from which a significant difference between the FE strain maps and simulated DIC strain maps can be observed. This finding shows that the systematic error originating from the low-pass spatial filtering effect of the DIC process has an important impact on the accuracy of the VFM identification. The optimal selection of the parameters of the DIC measurements (subset size, smoothing kernel) will be investigated later. In this study, the aim was to identify the best test configuration which leads to the minimum sensitivity to this systematic error. As illustrated by the C_1 contour maps (see Figures 8 and 9), the most stable and accurate identifications are found in the tensile test configuration region (α=90°) with off-axis angles ranging between 10° and 35°. In the actual experiments, it is difficult to control the off-axis angle θ accurately so the optimized test configuration for this study was selected to be θ=25° and α=90° which is close to the centre of the favourable region to ensure accuracy of the identified results. Figure 9(a) shows the C1 contour maps with a larger Gaussian kernel size of 10. By comparing the minima with the result in Figure 8(b) with less smoothing, it can be noted that the optimal configurations are found in the same region of the search space. In addition, this test configuration confirms the results from the previous study using FE strains [17] (shown in Figure 9(b)), even though another good potential candidate at (θ=35° and α=30°) was found in that study, which is clearly discarded with the present approach. The current study also provides a much more

realistic evaluation of the expected identification error. As can be observed from Figures 8(b) and 9(a), the level of predicted error on the identification is increased from 0.01 to 0.06 by including the DIC simulation.

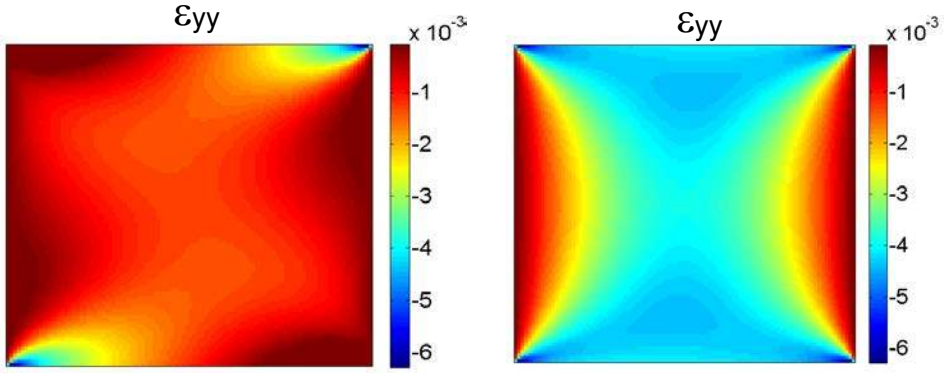

(a) (b)

Figure 10: FE ε_{yy} strains for (a) θ=5° and α=60°; (b) θ=25° and α=90°

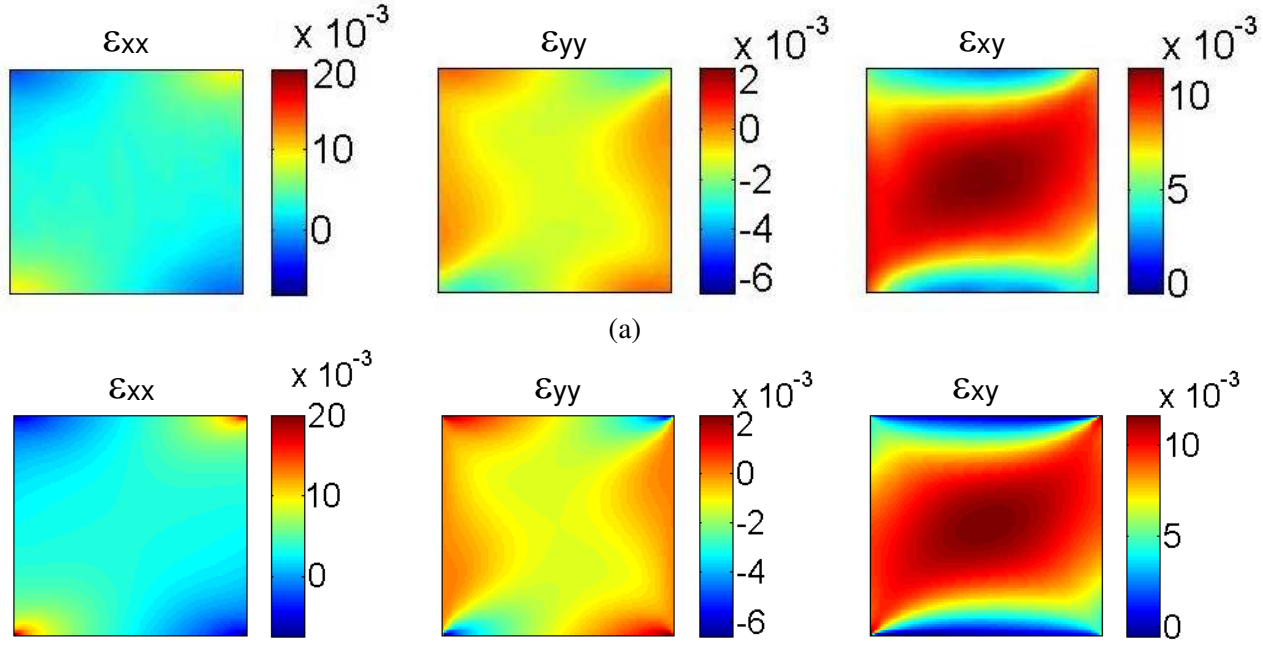

(a)

(b)

Figure 11: (a) Strain maps from simulated DIC using synthetic images without noise (subset 30, Gaussian smoothing kernel size of 10, θ=5° and α=60°);
(b) Strain maps from FE model (θ=5° and α=60°).

The error functions corresponding to each identified material stiffness parameters Q_{11}, Q_{12}, Q_{22} and Q_{66} are plotted separately in Figure 12. The results indicate that the systematic error is the largest for Q_{22} and Q_{12}. This

was expected as transverse strains tend to concentrate near the corners of the specimen for most Arcan test specimen configurations. The identification accuracy of the Q_{11} and Q_{22} parameters mainly depends on the off-axis angle of the specimens. When the loading direction α is aligned with the stiffness component direction (θ=0° for Q_{11} and θ=90° for Q_{22}), the best identification of these two components is obtained. The off-axis tensile test configuration provides balanced identification of the four stiffness components.

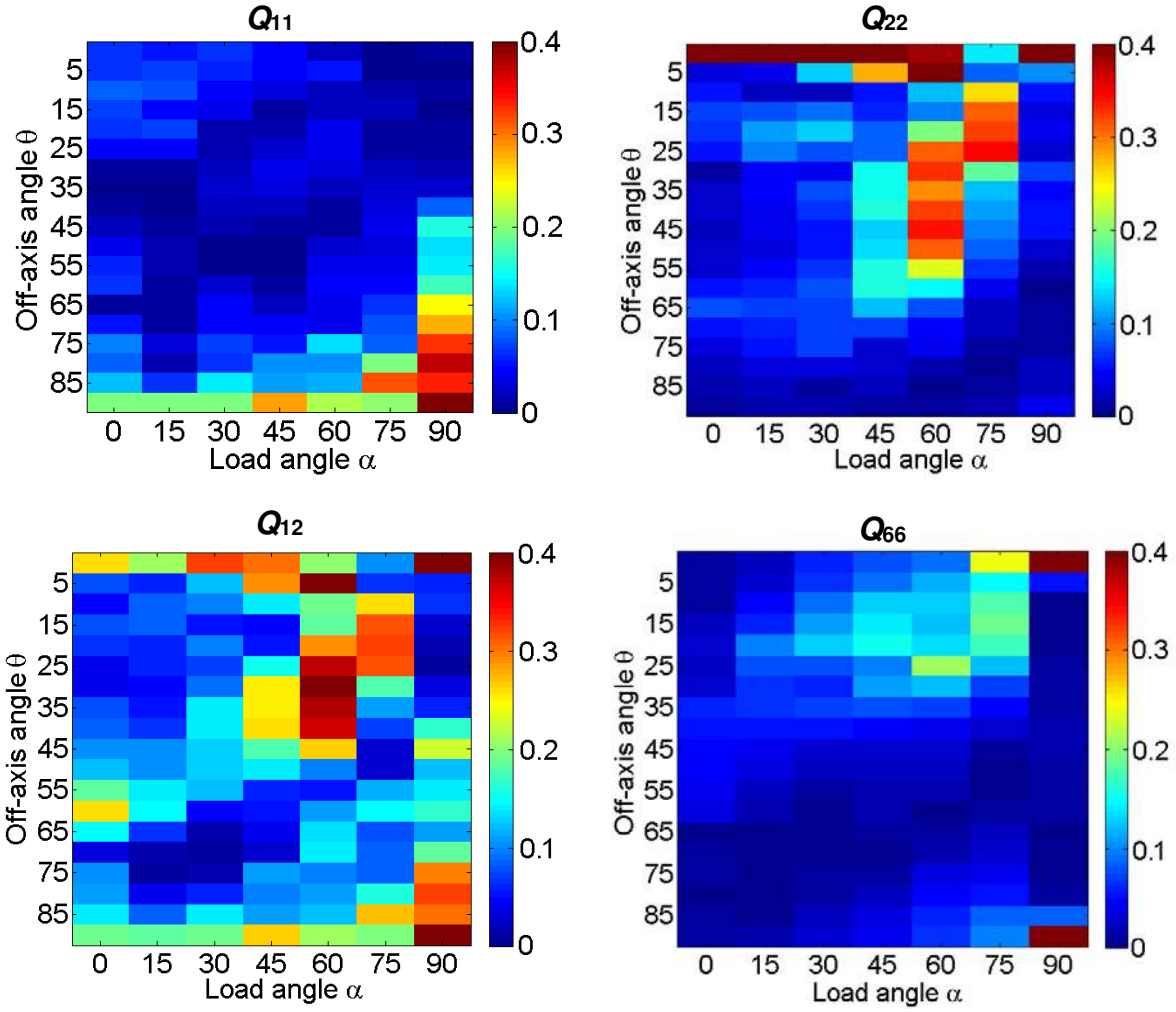

Figure 12: Relative error for each of the identified material parameters (Q_{11}, Q_{12}, Q_{22} and Q_{66}) after reconstructing the missing data on the edges of the specimen, subset 30, Gaussian smoothing kernel size of 10.

In the next section, the optimization of the DIC parameters (subset size, Gaussian smoothing kernel size) will be investigated to further improve the accuracy of the predicted error of the identification.

Besides the systemic error caused by the DIC process, another important identification bias can be introduced by the through-thickness stress and strain heterogeneity which is neglected when using the plane stress assumption in the VFM routine (namely when volume integrals are approximated by the thickness multiplied by a surface integral in the principle of virtual work). To check for this, a full 3D FE model was built up and the surface displacements from this model were input into the identification simulator. The optimized test configuration (θ=25° and α=90°) from the above systematic error study was used in this model. The identified parameters are compared with the results using 2D FE model so that the error related to this through-thickness heterogeneity can be isolated, as the 2D FE model results already capture the DIC-based errors. The identification biases are listed in Table 2. It can be seen that although the thickness of the specimen is only a fourth of its in-plane dimensions, there is still a slight over-estimation of the identification parameters. By further reducing the thickness, this identification bias can be decreased. However, a much thinner specimen would be easily damaged during the mounting of the specimen in the fixture. So it is more practical to keep this specimen thickness and correct for this bias..

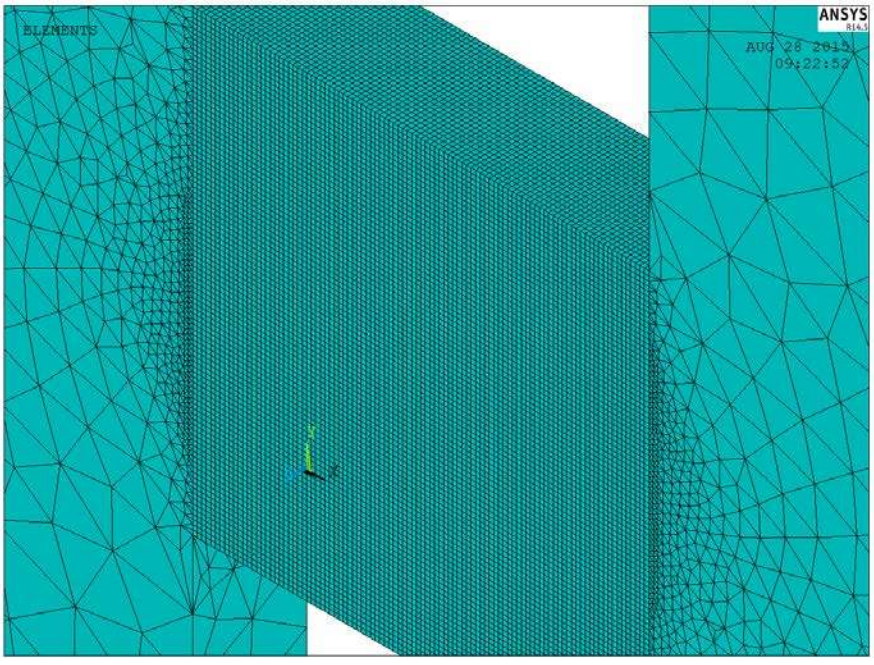

Figure 13: 3D FE model of the modified Arcan test

Table 2: Identification bias due to through-thickness strain heterogeneities

	Q11	Q22	Q12	Q66
3D FE model	148.4	67.8	29.4	31.8
2D FE model	146.3	66.2	28.2	31.1
Identification bias	1.4%	2.4%	4.2%	2.3%
DIC systematic bias	2.1%	4.6%	7.2%	2.7%

Test optimization based on the random error

The random component of the identification error is mainly due to image noise propagating through the DIC and VFM processes. This causes dispersion of the identified results, especially if the signal to noise ratio is low. In this study, the noise has been simulated by adding standard Gaussian white noise to the grey level values of the synthetic images. The noise level is obtained from actual measurements by capturing two stationary images and then evaluating the standard deviation of the difference of the two images which is around 1% of the dynamic range. The random error of the identified parameters is quantified by the coefficients of variation of the identified stiffness distributions obtained from repeats of the identification process with different copies of the noise on the images. The coefficient of variation is defined as the ratio of the standard deviation to the mean to produce a scaled measure of scatter regardless of the different orders of magnitude of the stiffness components. The simulations for each test configuration were repeated 20 times to evaluate the standard deviation of the

identified parameters. The error function C_2 representing the average of the coefficients of variation of the four identified material parameters (Q_{11}, Q_{12}, Q_{22} and Q_{66}) has been defined as specified by Eq. (10):

$$C_2(\alpha,\theta) = \frac{1}{4}\sum_{ij}\frac{std_{ij}}{Q_{ijref}}, (ij = 11,22,12,66) \tag{10}$$

where (as before) α is the loading angle and θ is the off-axis angle of the material principal direction. Q_{ijref} represents the reference values of the four identified material stiffness parameters [5], and std_{ij} is the standard deviation of the identified parameters over 20 repetitions. Figure 14 shows the plot of the C_2 error function. The highest scatter can be observed for (α=90°, θ=90°). This can be expected as the test specimen has much lower stiffness along the in-plane direction (Q_{22}=63.41 MPa) compared with the through-thickness direction (Q_{11}=143.4 MPa). When the specimen is loaded along the 2-direction, the strain component in the 1-direction is very small and highly influenced by noise. As can be seen from Figure 14, the optimal test configurations with the lowest standard deviation are predicted to be located near the off-axis shear and off-axis tensile positions. The standard deviations of each stiffness component are plotted separately in Figure 15. The contour maps indicate a similar situation as shown in the plots in Figure 14. This confirms that balanced strain components with relatively large magnitudes can reduce both systematic and random errors. For the identification of Q_{11} and Q_{22}, the lowest scatter was obtained when the loading direction is aligned with the stiffness component direction, i.e. the 1 or 2-directions, respectively, for the two stiffness parameters. The identification of Q_{66} is the most stable. The reason for this is the relatively low value of this stiffness component (Q_{66}=30.12 MPa) which results in relatively larger strain values which are less affected by noise. When this is combined with the previous findings in the study of the systematic error, the optimal test configuration is confirmed to be the off-axis tensile test defined by α=90° and θ=25°. This test can be christened the 'Short Off-axis Tension' test (SOT test) and is potentially an excellent candidate to become a new standard test for orthotropic materials, including fibre composites, as it can be performed in a standard test machine. This will be investigated in the future.

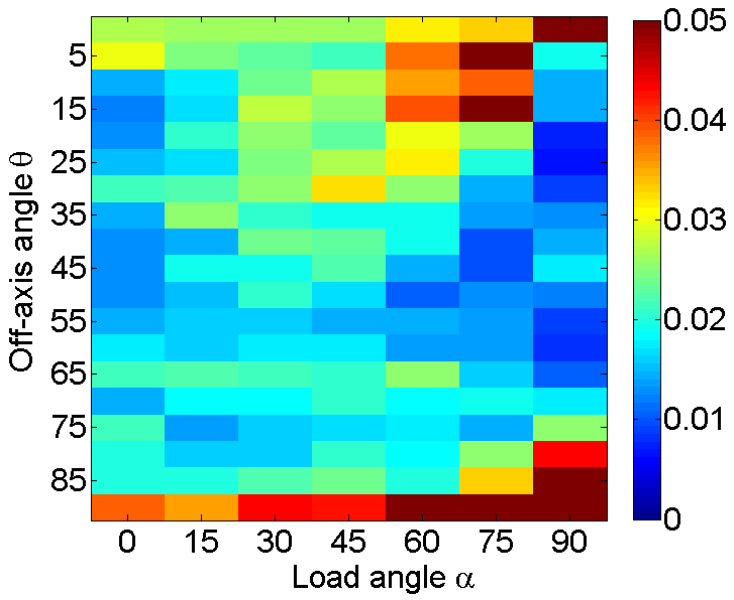

Figure 14: Error function C_2 (average coefficient of variation) with influence of measurement noise subset 30, Gaussian smoothing kernel size of 10.

Besides evaluating the standard deviation, the mean value of each identified parameter over 20 repetitions was also calculated. From this the identification error function C_1 can be recalculated as in eq. (11) with the mean of the distribution. For the sake of clarity, this cost function has been named C_3.

$$C_3(\alpha,\theta) = \frac{1}{4}\sum_{ij}\left(\frac{\left|\overline{Q}_{ij} - Q_{ijref}\right|}{Q_{ijref}}\right), (ij = 11,22,12,66) \qquad (11)$$

where $\overline{Q}_{ij}$ is the mean value of 20 repetitions, Q_{ijref} are the reference values of the four identified material stiffness parameters [5] input into the FE model, and (as before) α is the loading angle and θ is the off-axis angle of the material principal directions. The results are plotted in Figure 16, and it is observed that the contour map nearly coincides with the plot of the systematic error in Figure 8(b). This shows that the noise does not produce a significant additional bias.

Q_{11} Q_{22}

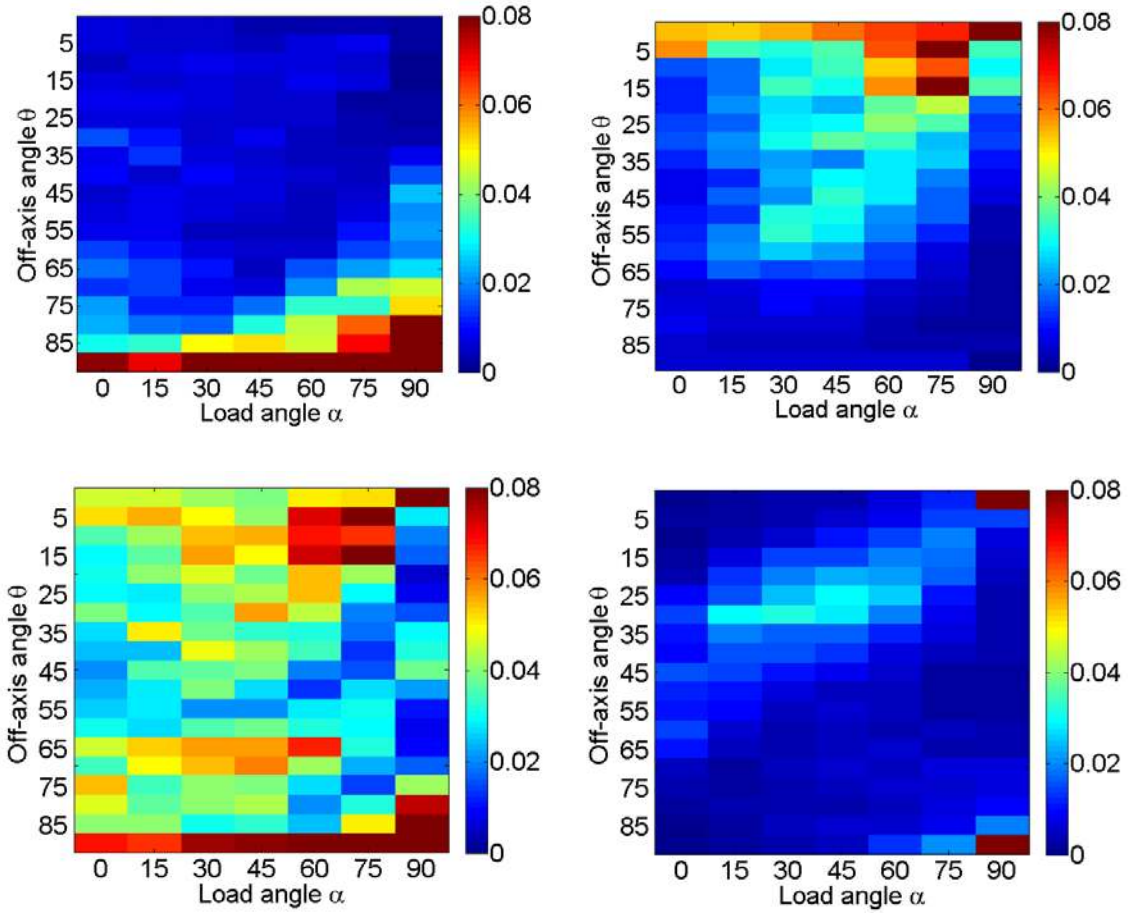

Figure 15: Coefficients of variation of the identified results over 20 repetitions, subset 30, Gaussian smoothing kernel size of 10.

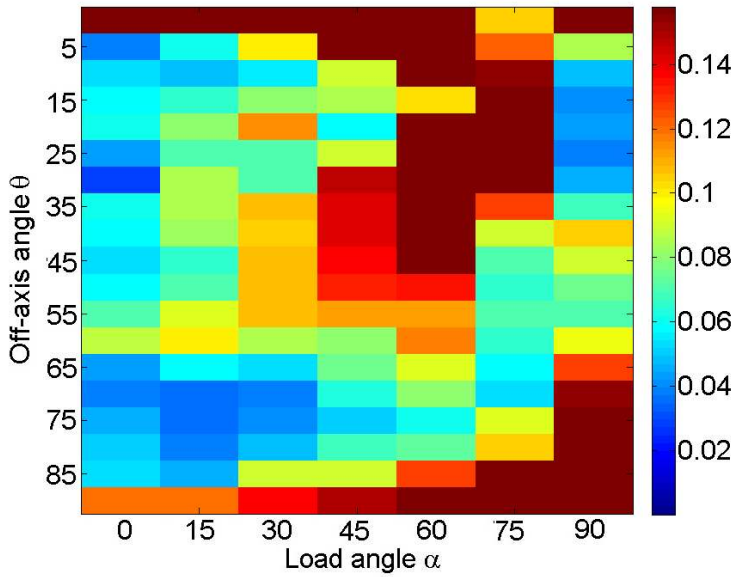

Figure 16: Error function C_3 (mean value of identified results over 20 repetitions), subset 30, Gaussian smoothing kernel size of 2

Selection of subset sizes and smoothing levels

In accordance with the results from the study of the systematic and random errors, the 'Short Off-axis Tension' (SOT) configuration (θ=25°, α=90°) has been selected as the optimal one for conducting physical experiments. As was discussed before, the DIC process strongly influences the quality of the measured strain maps and can lead to a significant bias on the VFM identification. It is therefore important to systematically study the effect of the main DIC parameters (subset size, smoothing kernel) and define optimal values for these. This enables a more rational approach to these important choices which directly impact the quality of the results. Therefore, different subset sizes (from 10 to 50) were adopted here to study the optimal choice of subset size based on the optimized test configuration. Spatial smoothing of the displacements is generally necessary to improve the strain resolution, particularly in the low elastic strain range considered here. However, while reducing the random component of the error, smoothing can significantly increase the systematic part of the error as was shown earlier in this article. At a certain stage, the systematic error overtakes the random error, so there is an optimal point somewhere. Therefore, the optimal choice of these two test parameters will be investigated by evaluating the overall identification error of the four identified stiffness parameters with different smoothing levels (kernel

sizes) and subset sizes. The smoothing technique adopted here is Gaussian smoothing of the strain maps. Other types of smoothing could have been investigated but it is thought that the regularization parameter (kernel size here) is more important than the actual smoothing technique used as they all provide some low pass filtering which cut-off frequency is driven by the regularization parameter. The results will be compared to the reference values (Q_{11}=143.4 MPa, Q_{22}=63.41 MPa, Q_{12}=26.01 MPa, Q_{66}=30.12 MPa) [5]. A way to define the optimal point (smallest error) is to consider a 95% confidence interval. This is the mean plus or minus twice the standard deviation. Therefore, the largest possible error, with a 95% confidence, is obtained as follow: if the mean is below the reference, it will be the mean minus twice the standard deviation; if the mean is above the reference, then it will be the mean plus twice the standard deviation. By plotting this maximum error, the optimal parameters and a confidence interval are identified. The error function is defined in eq. (12). The variables used here are the subset and kernel sizes.

$$C_4(sub,\ker) = \frac{1}{4}\sum_{ij}\left(\frac{\max\left|Q_{ij}^C - Q_{ijref}\right|}{Q_{ijref}}\right), (ij = 11,22,12,66) \tag{12}$$

where Q_{ijref} are the reference values of the four material stiffness parameters [5] input into the FE model, Q_{ij}^C are the stiffness parameters with 95% confidence interval which is defined in eq. (13)

$$Q_{ij}^C(sub,\ker) = \overline{Q}_{ij} \pm 2std_{ij}, (ij = 11,22,12,66) \tag{13}$$

where $\overline{Q}_{ij}$ is the mean of the four stiffness parameters over 20 repetitions calculated with different subset and kernel sizes and std_{ij} is the standard deviation of the four stiffness parameters over 20 repetitions.

First, it is possible to evaluate the systematic part of the error by evaluating C_4 without any noise. This leads to the systematic error reported in Figure 17. As expected, this error increases for increasing subset sizes and smoothing levels. Then, adding noise, it is possible to evaluate the random part of the error by subtracting the systematic error from the total error obtained from C_4 with noise. This part of the error increases moderately with decreasing subset size, and decreases more sharply with increasing smoothing levels. At some stage, these

two curves cross-over, showing that there should be an optimum. This optimum is clearly seen on Figure 18 which shows that kernel size equal to 11 and subset size is 40x40.

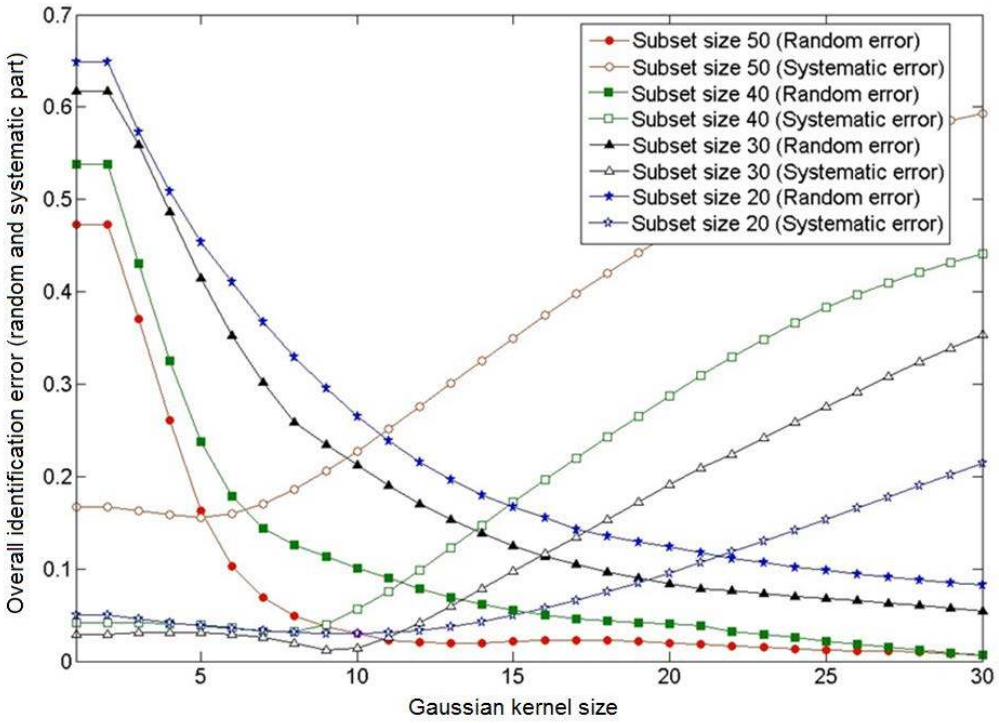

Figure 17: Systematic and random errors

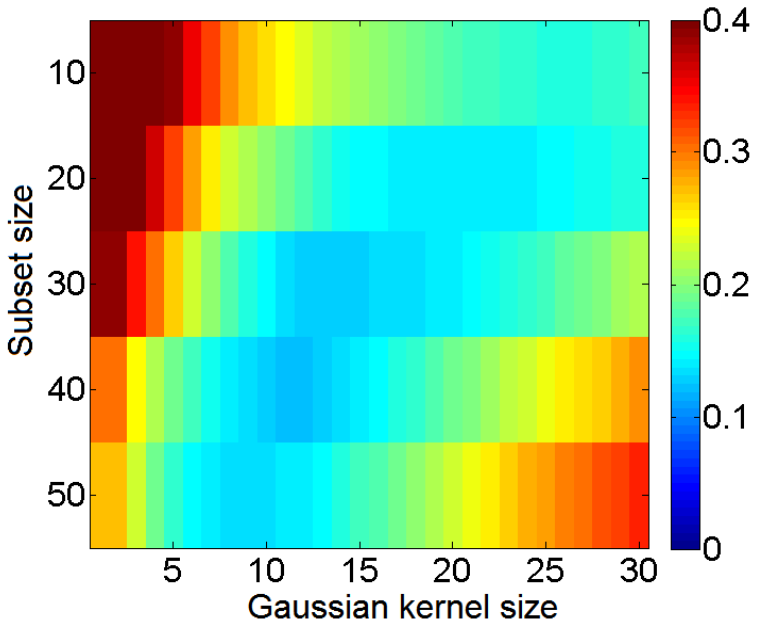

Figure 18: Error function C_4 with different subsets and Gaussian smoothing kernel sizes

Confidence interval and effect of image averaging

With the systematic and random errors predicted from the simulated measurements, confidence intervals can be calculated to indicate the reliability of the identification. The confidence interval of each identified stiffness parameter is defined as follows corresponding to a 95% confidence level:

$$CI_{ij}=Q_{ij}\,(without\ noise)\pm 2std_{ij}\,(standard\ deviation\ with\ noise),\ (ij=11,22,12,66) \quad (14)$$

The averaging of multiple static images may provide an efficient way to reduce the data dispersions caused by image noise. In a practical testing context when the specimen is loaded up to a certain level and stabilized, it is possible to record many images and then average them to filter out camera noise. The effect of image averaging has been further investigated using the optimized test parameters determined from the above study. The confidence intervals of the four stiffness parameters determined by averaging based on different numbers of images (5, 10, 20, 50, and 100) have been calculated individually. The results are plotted in Figure 19, where the black dots show the upper limits of the confidence interval and the red dots represent the lower limits. As expected, the confidence intervals reduce when the number of images is increased. This phenomenon demonstrates that the averaging of multiple stabilized images exerts an influence on the identification. Thus, by utilising this procedure instead of increasing the smoothing level, the random error can be effectively reduced without raising the systematic bias. Furthermore, the results also indicate that the elastic stiffness parameters tend to converge to values that are slightly larger than the reference values. This is due to the systematic error originating from the low pass filtering effect of the DIC process. Although the random error of the measurement is significantly reduced, the systematic bias still exists and results in an over-prediction of the stiffness parameters. When the number of images exceeds 50, the confidence interval stabilizes, and the optimal number of images was therefore set to 50.

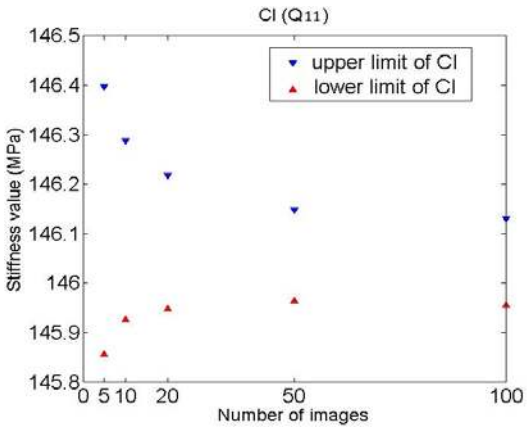

(a) CI_{11} (Reference Q_{11}=143.4 MPa)

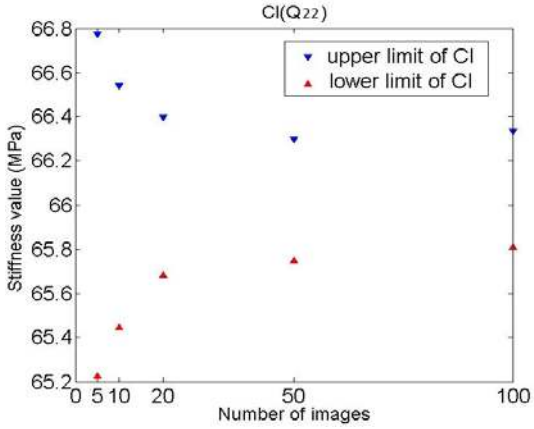

(b) CI_{22} (Reference Q_{22}=63.41 MPa)

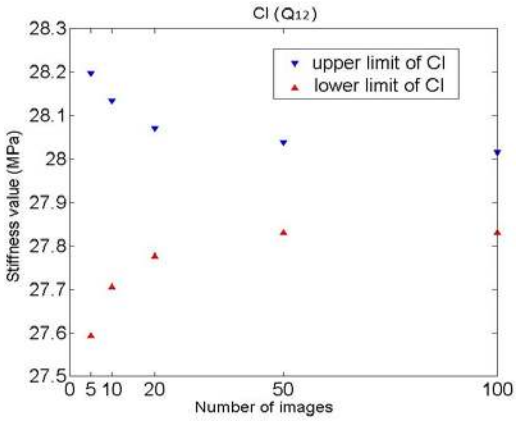

(c) CI_{12} (Reference Q_{12}=26.01 MPa)

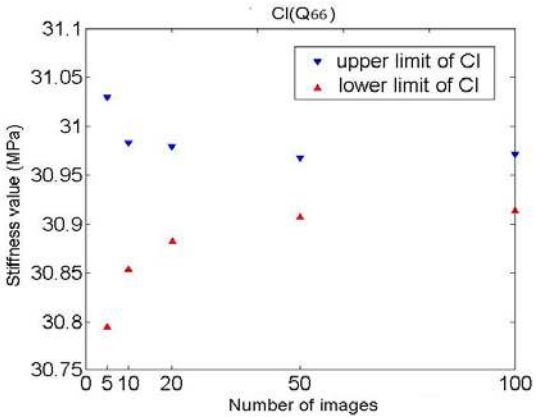

(b) CI_{66} (Reference Q_{66}=30.12 MPa)

Figure 19: Confidence intervals (*CI*s) of the four stiffness parameters.

Experimental validation

The SOT experiments (Figure 20) were conducted using 3 different but identical specimens, and the testing was set up according to the optimized configuration selected from the numerical study. The stiffness parameters can be calculated in two different ways. One way is to firstly average out the displacements and then perform the VFM identification. Another way is to perform two VFM identifications on each side of the specimens and average the identified results. A study was performed to compare the results from these two approaches (shown in Table 3). It can be seen that the two approaches gave almost the same results. There is a small difference which might due to the variations of the speckle patterns or lighting conditions on each side of the specimens. The results indicate that averaging the identified results or the measured displacements from each side of the

specimen can eliminate the effect of out-of-plane movements and provide the same stiffness results. In the following study, the measured displacements were averaged firstly. Then the stiffness parameters were identified from the VFM routine afterwards.

Table 3: Comparison of identification results from two approaches (averaging the measured displacements or averaging the identification results from the two sides of the specimen)

	Q_{11} [MPa]	Q_{22} [MPa]	Q_{12} [MPa]	Q_{66} [MPa]
Identification results from the frontside of the specimen	167.16	73.50	36.85	32.83
Identification results from the backside of the specimen	136.94	63.72	22.81	31.98
Average of the front and back stiffness results	152.05	68.61	29.83	32.41
Identification results from averaged displacements	150.69	69.43	28.63	32.46

Subset size and smoothing kernels were selected to be 40 and 10 according to the systematic study previously reported. The detailed performance of this setup is given in Table 4. The resolutions were evaluated as the standard deviation of the displacement and strain maps of two consecutive images of the stationary specimen. In order to validate the effect of image averaging, the experiments were conducted by capturing single and multiple images of the stabilized specimens. To ensure that the specimens were not loaded beyond the range of linear elasticity, they have been subjected to loads up to only 100N which is the load level used for the simulations in this configuration. After around 30 s when the specimen has stabilized (stable force reading), multiple images were captured with the rate of one image per second. This measurement procedure was then repeated 20 times on the same day and the specimen was kept in the fixture/machine during the process. Both the mean value and the standard deviation of the identified material stiffness parameters were then calculated, and the results were subsequently compared with both the simulated data and the reference experimental data.

The simulation data was also calculated based on the same realistic images captured in this experiment. The reference values for the elastic properties were obtained using ASTM standard tests in [5], as well as from measurements conducted using the modified Arcan fixture with tensile tests along the in-plane and through-thickness directions and shear tests using butterfly-shaped specimens [6]. The reference values reported in [5] and [6] are very similar.

Table 4: Experimental DIC settings and performances (MatchID DIC package).

Technique Used	2D image correlation
Subset size	40 x 40 pixel^2
Shift	20 pixel (50%)
Shape function	Affine
Interpolation function	Bicubic polynomial
Correlation criterion	Approximated Normalized Sum of Squared Difference (Approximated NSSD)
Presmoothing applied to the images	None
Camera	8 bit, 2048 x 2048 pixel^2
Field of view	24mm x 24mm
Displacement field:	
Resolution	0.2 μm / 0.017 pixel
Strain field:	
Differentiation method	Finite differences
Smoothing method	Gaussian smoothing (kernel size 11)
Resolution	1.3×10^{-4}

Figure 20: Short Off-axis Tensile (SOT) test experimental set up.

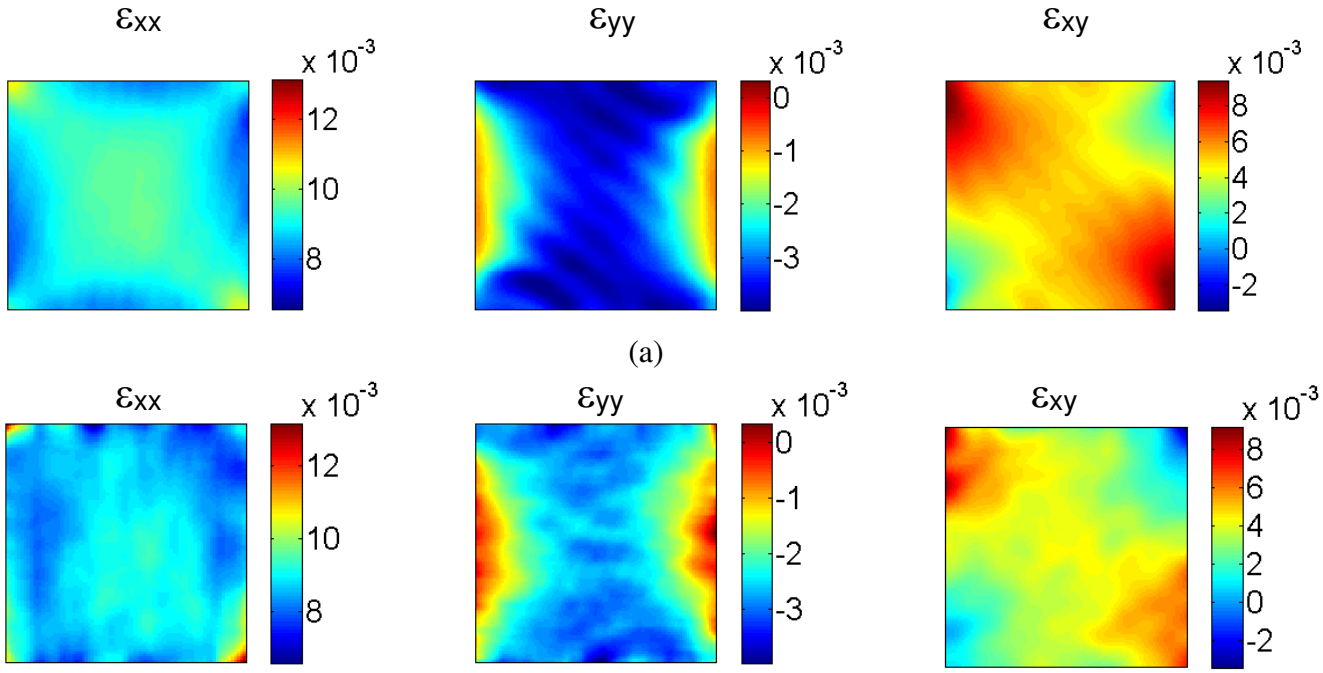

Figure 21: (a) Strain maps from DIC simulations (subset 40x40, smooth kernel 11, 100N); (b) Strain maps from physical experiments (the average of two back-to back cameras, subset 40x40, smooth kernel 11, 100N)

The simulated DIC strain maps and strain maps obtained from the physical DIC experiments are shown in Figure 21, from which a good correlation is observed between the two sets of data. The mean values of the identified stiffness components obtained over 20 repetitions using 50 averaged images are listed in Table 5.

Table 5: The mean value from 20 repetitions using 50 average images.

	Q_{11} [MPa]	Q_{22} [MPa]	Q_{12} [MPa]	Q_{66} [MPa]
Specimen 1	149.3	68.1	27.9	32.9
Specimen 2	147.6	70.8	29.6	31.1
Specimen 3	150.1	69.1	29.9	32.4
Mean value	149.0	69.3	29.1	32.1
DIC Simulation	146.1	66.0	27.9	30.9
Reference data [5]	143.4	63.4	26.0	30.1

Table 6: The standard deviation and coefficients of variation from 20 repetitions using 50 averaged images.

	Q_{11} [MPa]	Q_{22} [MPa]	Q_{12} [MPa]	Q_{66} [MPa]
Specimen 1	0.169	0.646	0.225	0.132
Specimen 2	0.155	0.623	0.203	0.133
Specimen 3	0.223	0.715	0.250	0.159
Mean value	0.182	0.661	0.226	0.131
DIC Simulation	0.0458	0.138	0.0520	0.0152
Coefficients of variation				
Experimental	0.12%	0.95%	0.78%	0.41%
DIC simulation	0.030%	0.20%	0.18%	0.047%

Table 7: The standard deviation and coefficients of variation from 20 repetitions using one single image.

	Q_{11} [MPa]	Q_{22} [MPa]	Q_{12} [MPa]	Q_{66} [MPa]
Specimen 1	0.345	1.42	0.302	0.251
Specimen 2	0.389	1.39	0.295	0.230
Specimen 3	0.413	1.62	0.337	0.278
Mean value	0.382	1.48	0.311	0.253
DIC Simulation	0.275	0.993	0.205	0.122
Coefficients of variation				
Experimental	0.25%	2.1%	1.07%	0.79%
DIC simulation	0.18%	1.5%	0.73%	0.39%

The simulated DIC experiments provide a good prediction of the results obtained from the physical measurements. Both the experimental and the simulated results display larger mean values of the identified material parameters than the set of reference data. This demonstrates that the systematic error of the DIC process causes an over-prediction of the stiffness parameters because of the smoothing out of local strain peaks. The material parameters identified from the physical experiments display slightly larger mean values than that predicted using the simulated DIC procedure. This is not surprising as other sources of error come into play like non-uniform lighting or lens distortions [26]. Tables 4 and 5 provide the standard deviations and coefficients of variation of the identified results over 20 repetitions using either the average of 50 images or a single image. The results using the average of 50 images display a significant reduction of the standard deviation of the 20 repeated measurements. However, the efficiency of this method in the experiments is not as significant as was suggested by the results of the numerical study, and the resulting standard deviation has not come down to the expected value.

In order to further investigate the cause of this deviation, the difference of the grey level intensity between two consecutive images is compared with the average of different numbers of images. The evolution of the noise level by averaging different numbers of stabilized images is illustrated in Figure 22. As demonstrated in the

study based on the simulated DIC procedure (shown in Figure 21(a)), the noise effect is seen to gradually reduce when the number of images that are used in the averaging is increased. However, by evaluating the images from the physical measurements, the situation is not quite the same as that observed from the predictions of the simulated experiments. It can be seen that when taking up to 10 images and averaging them, the noise influence is reduced as in the numerical prediction. However, by taking images continuously up to 50 the noise is seen to increase again. This is the reason why the standard deviation of the experimental results is not significantly reduced using the optimal number of images (50). This phenomenon indicates that the specimen was not experiencing static steady state conditions when the recording of the multiple images was conducted. Since the integration time was one second per image, this indicates that the patterns on the surface of the specimen may have displayed a slight variation after 10 seconds. A likely explanation for this time-dependency problem is that the PVC foam material displays viscoelastic behaviour, hence creep can occur over 50 seconds even when one thinks that the load is stabilized. Other effects like changes of lighting conditions or air movements can also play a role. Furthermore, camera heating is also a important aspect, A way to resolve this issue would be to increase the rate of image acquisition to reach the optimal number of images within 10 seconds. Table 8 displays the standard deviation calculated using 10 instead of 50 images. Comparing with the data in Table 6, the difference between the test results and the predicted standard deviation from DIC simulation is significantly reduced.

Table 8: The standard deviation from 20 repetitions using 10 averaged images.

	Q_{11} [MPa]	Q_{22} [MPa]	Q_{12} [MPa]	Q_{66} [MPa]
Specimen 1	0.118	0.403	0.138	0.0689
Specimen 2	0.095	0.363	0.117	0.0534
Specimen 3	0.132	0.471	0.152	0.0692
DIC Simulation	0.0701	0.235	0.0914	0.0376

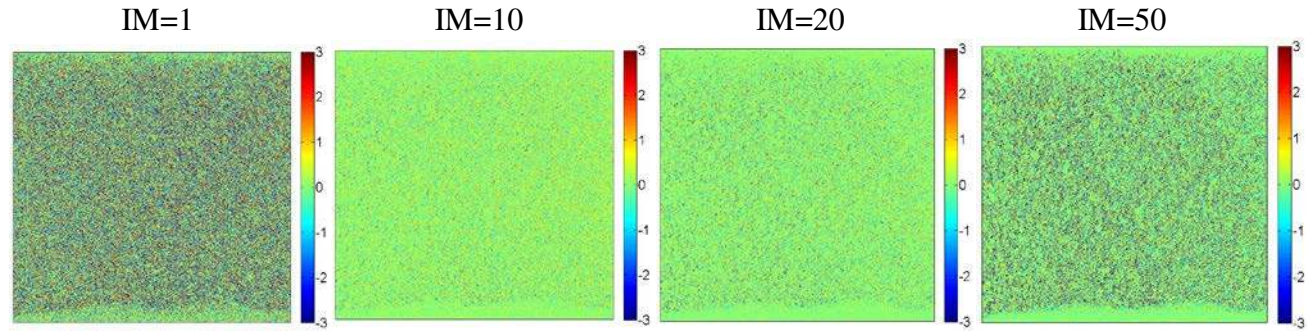

(a)

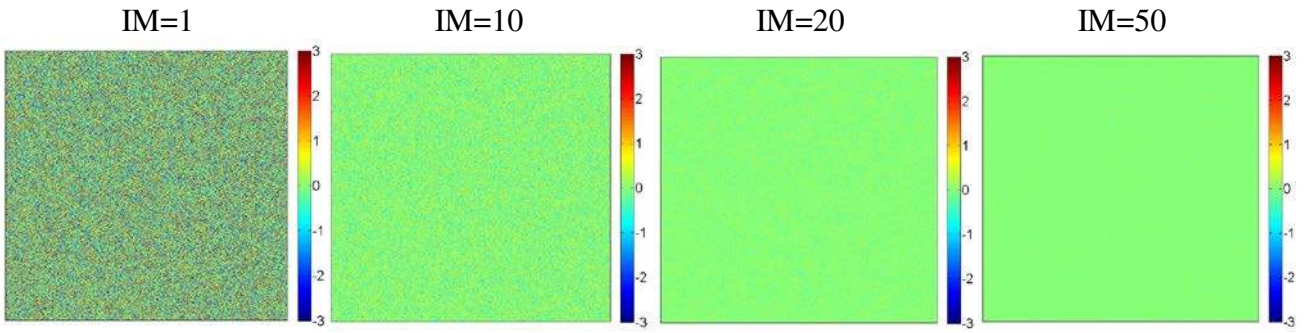

(b)

Figure 22: The noise level (in grey level values) of the images using either a single image (IM=1) or the average of multiple images: (a) based on the results of the physical experiments; (b) based on simulation.

Conclusion

In this paper, a methodology has been developed to predict the uncertainty of the experimental characterisation of cross-linked PVC orthotropic foam materials and to optimize the design of the experiments. Optimal test parameters have been sought to provide a reliable identification of all the elastic stiffness parameters in one single test using Digital Image Correlation and the Virtual Fields Method. The image recording from physical experiments was mimicked by deforming the reference speckle patterns using displacements derived from FE analysis. DIC and VFM routines were used to process the synthetic speckle patterns and to extract all the elastic stiffness parameters. By using this method, a large number of simulated experiments were generated efficiently with varying testing parameters. For the current study, the test parameters selected were the loading angle (α), the off-axis angle (θ) to the material principal direction, the subset size and the smoothing kernel. Several error

functions have been defined to describe both the systematic and random errors on the VFM identified results. Based on this, an optimum test configuration was identified by minimizing the identification error.

The main conclusions of the present article can be listed as follows:

1. The study of the systematic error has demonstrated that the low pass filtering effect of the DIC process can bring significant bias to the identification results. By using the simulated DIC measurements, this error source can be included into the optimization study and also provide a more realistic prediction of the expected identification error. It was further observed that the random error can be reduced by averaging over multiple images. By combining the results from the analyses of the systematic and random errors, a Short Off-axis Tensile (SOT) test (θ=25°, α=90°) was chosen as the optimized test configuration.
2. Based on the optimized test configuration, several optimal test parameters related to the DIC process were determined. The results showed that increasing the subset size and the smoothing level exerted opposite effects on the systematic and random errors of the VFM identification. It is therefore important to balance out the two different sources of error when choosing the optimal DIC processing parameters.
3. The confidence interval of the parameters obtained from the simulation was calculated based on the systematic and random errors. The study of image averaging revealed that the confidence intervals tend to stabilize when the number of images used in the averaging is increased, whereas the systematic error remains unchanged and causes over-prediction of the identified material parameters.
4. Finally, the predictions of the simulated experiments in terms of identified material parameters have been validated against physical experiments. From this it was further concluded that the simulated measurement procedure can provide a realistic quantification of the identification error, and also that the optimized testing configuration and DIC parameters led to a stable and accurate parameter identification. However, when using the average of the optimal number of images, the random error of the experimental results was not reduced as effectively as was predicted from the simulated experiments. The reason for this is probably the lack of stability of the imaging conditions during the image recording process. To reduce this error, a

higher frame rate would be required to capture the optimal number of images within as short a time as possible.

Finally, one must emphasize that many additional error sources were not considered in the present work, for instance, slight misalignment between the specimen surface and the camera sensors, non uniform lighting and light noise from the environment. This explains the limited differences that still exist between the predicted and actual confidence intervals. A follow-up on this work will be to include such errors and perform a sensitivity analysis.

This work is a step towards new standard tests based on full-field measurements and inverse identification which will enable faster and more cost-effective material testing in the future. There are still a few steps left towards this goal but it is getting closer. A key issue is the systematic error but this will soon be mitigated by the availability of affordable high quality, high spatial resolution (16 Mpixels) and low noise (sCMOS) cameras. The last step is to make all the elements of this procedure robust to routine use by non experts. This work is currently underway and will be reported in the future.

Acknowledgement

The research reported was sponsored by the Innovation Fund Denmark through the project “Advanced Thermal Breaker”, which has been carried out in close collaboration with Fiberline Composites A/S, Denmark. The financial support is gratefully acknowledged. Prof. Pierron acknowledges the support of the Wolfson Foundation and the Royal Society through a Royal Society Wolfson Research Merit Award.

References

1. Gdoutos EE, Daniel IM, Wang KA (2001) Multiaxial characterization and modeling of a PVC cellular foam. *J. Thermoplast. Compos. Mater*. 14(5):365–373

2. Kanny K, Mahfuz H, Thomas T, Jeelani S (2004) Static and dynamic characterization of polymer foams under shear loads. *J. Compos. Mater*. 38(8):629–639

3. Kabir ME, Saha MC, Jeelani S (2006) Tensile and fracture behavior of polymer foams. *Mater. Sci. Eng. A*. 429(1–2):225-235

4. Daniel I, Cho JM (2011) Characterization of anisotropic polymeric foam under static and dynamic loading. *Exp. Mech*. 51(8): 1395-1403

5. Zhang S, Dulieu-Barton JM, Fruehmann R, Thomsen OT (2012) A Methodology for obtaining material properties of polymeric foam at elevated temperatures. *Exp. Mech*. 52 (1), 3-15

6. Taher ST, Thomsen OT, Dulieu-Barton JM, Zhang S (2011) Determination of mechanical properties of PVC foam using a modified Arcan fixture. *Composites Part A*. 43(10), 1698-1708

7. DIAB (2011) Divinycell PVC datasheet. http://www.diabgroup.com

8. Geymonat G, Hild F, Pagano S (2002) Identification of elastic parameters by displacement field measurement. *CR. Mecanique*, 330 (6), 403-408

9. Claire D, Hild F, Roux S (2002) Identification of damage fields using kinematic measurements. *CR. Mecanique*, 330 (11), 729-734

10. Pierron F, Grédiac M (2012) The Virtual Fields Method. Springer New York. ISBN 978-1-4614-1823-8

11. Chu TC, Ranson WF, Sutton MA, Peters WH (1985) Applications of digital image correlation techniques to experimental mechanics. *Exp. Mech.*, 25 (3), 232-244

12. Bruno L, Poggialini A (2005) Elastic characterization of anisotropic materials by speckle interferometry. *Exp. Mech.*, 45 (3), 205-212

13. Surrel Y (1994) Moiré and grid methods: a signal processing approach. *Proceedings of SPIE*, 2342, 213-220

14. Pierron F, Vert G, Burguete R, Avril S, Rotinat R, Wisnom M (2007) Identification of the orthotropic elastic stiffnesses of composites with the virtual fields method: sensitivity study and experimental validation. *Strain*, 43(3), 250-25

15. Syed-Muhammad, K., Toussaint, E., Grédiac, M. (2009) Optimization of a mechanical test on composite plates with the virtual fields method. *Struct. Multidiscip. O.,* 38(1), 71-82.

16. Rossi M, Pierron F (2012) On the use of simulated experiments in designing tests for material characterization from full-field measurements. *Int. J Solids Struct.* 49 (3-4), 420-435

17. Wang P, Pierron F, Thomsen OT (2013) Identification of material parameters of PVC foams using Digital Image Correlation and the Virtual Fields Method. *Exp. Mech*. 53(6): 1001-1015

18. Moulart, R., Avril, S., Pierron, F. (2006). Identification of the through-thickness rigidities of a thick laminated composite tube. *Composites Part A*, 37(2), 326-336.

19. MatchID – www.matchid.org (last accessed 29th July 2014)

20. Lava P, Cooreman S, Coppieters S, Strycker MD, Debruyne D (2009) Assessment of measuring errors in DIC using deformation fields generated by plastic FEA. *Opt Lasers Eng*. 47: 747-753

21. Rossi M, Lava P, Pierron F, Debruyne D, Sasso M (2015) Effect of DIC spatial resolution, noise and interpolation error on identification results with the VFM, *Strain,* in revision.

22. Robert MJ (1998) Mechanics of composite materials. CRC Press. ISBN-10: 156032712X.

23. Toussaint E, Grédiac M, Pierron F (2006) The virtual fields method with piecewise virtual fields. *Int. J. Mech. Sci.*, 48(3), 256-264.

24. Avril S, Grédiac M, Pierron F (2004) Sensitivity of the virtual fields method to noisy data, *Comp. Mech.*, 34(6):439-452.

25. Evaluation of measurement data — Guide to the expression of uncertainty in measurement, JCGM 100:2008 http://www.bipm.org/utils/common/documents/jcgm/JCGM_100_2008_E.pdf (last accessed on July 29th 2014)

26. Lava, P., Van Paepegem, W., Coppieters, S., De Baere, I., Wang, Y., Debruyne, D. (2013). Impact of lens distortions on strain measurements obtained with 2D digital image correlation. *Optics and Lasers in Engineering, 51,* 576-584

Appendix

The stress/strain curves based conventional mechanical method has been reported in the Appendix. The different shapes of test specimens were designed for the MAF test rig: a butterfly shaped (BS) specimen geometry for shear, a short dogbone (SD) specimen geometry for tensile loading, These curves have been published previously. It has been referenced in this paper also (ref [6], Taher ST, Thomsen OT, Dulieu-Barton JM, Zhang S (2011) Determination of mechanical properties of PVC foam using a modified Arcan fixture. Composites Part A. 43(10), 1698-1708). The stress/strain curves are shown in the Figures 23. It can be seen that the behaviour of the material remains linear in a range between -1% to 1% strains.

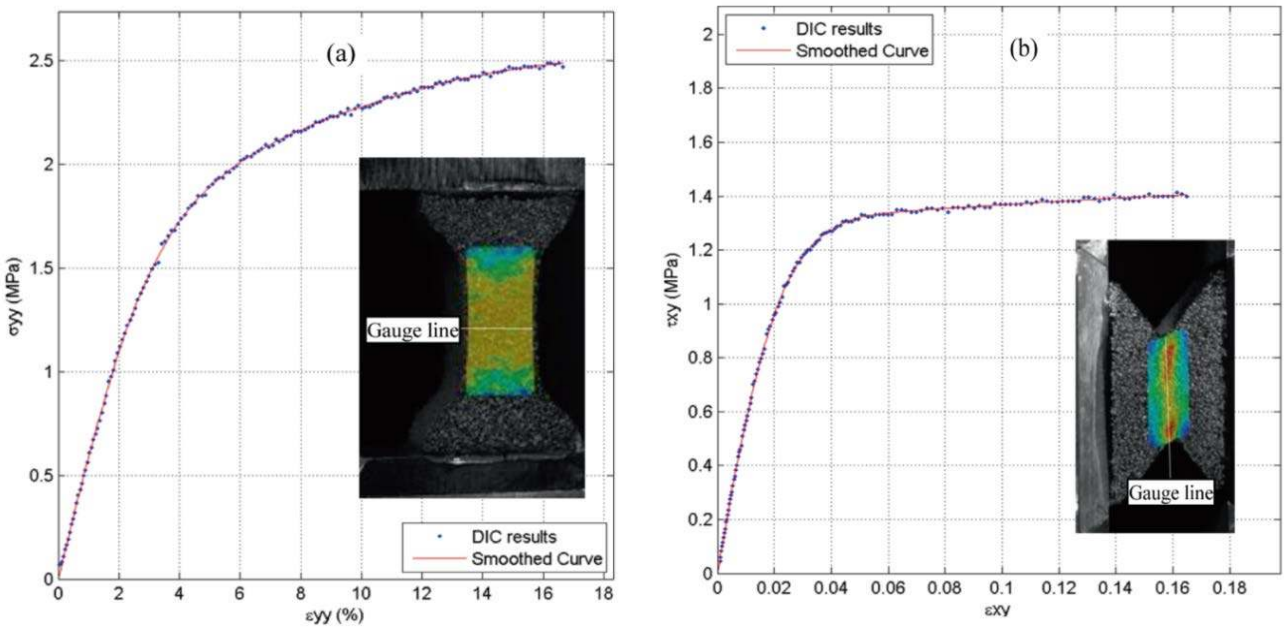

Figure 23: The stress/strain curves of PVC foam materials based conventional mechanical method [6]